Award Number: W81XWH-12-2-0038

TITLE: Prevention of Blast-Related Injuries

PRINCIPAL INVESTIGATOR: Albert I. King

CONTRACTING ORGANIZATION: Wayne State University
Detroit, MI 48202

REPORT DATE: July 2013

TYPE OF REPORT: Annual

PREPARED FOR: U.S. Army Medical Research and Materiel Command
Fort Detrick, Maryland 21702-5012

REPORT DOCUMENTATION PAGE

Form Approved
OMB No. 0704-0188

1. REPORT DATE	2. REPORT TYPE	3. DATES COVERED
July 2013	Annual	15 June 2012 to 14 June 2013

4. TITLE AND SUBTITLE
Prevention of Blast-Related Injuries
2012-2013 Annual Report

5a. CONTRACT NUMBER
W81XWH-12-2-0038

5b. GRANT NUMBER
W81XWH-12-2-0038

5c. PROGRAM ELEMENT NUMBER

6. AUTHOR(S)
Albert King, John Cavanaugh, King Yang, Liying Zhang, Xin Jin, Feng Zhu

E-Mail: king@rrb.eng.wayne.edu

5d. PROJECT NUMBER

5e. TASK NUMBER

5f. WORK UNIT NUMBER

7. PERFORMING ORGANIZATION NAME(S) AND ADDRESS(ES)
Wayne State University

Detroit, MI 48202-3692

8. PERFORMING ORGANIZATION REPORT NUMBER

9. SPONSORING / MONITORING AGENCY NAME(S) AND ADDRESS(ES)
U.S. Army Medical Research and Materiel Command
Fort Detrick, Maryland 21702-5012

10. SPONSOR/MONITOR'S ACRONYM(S)

11. SPONSOR/MONITOR'S REPORT NUMBER(S)

12. DISTRIBUTION / AVAILABILITY STATEMENT
Approved for Public Release; Distribution Unlimited

13. SUPPLEMENTARY NOTES

14. ABSTRACT
This report covers work done in preparation for open field blast testing of swine and post-mortem human subjects as well as the development of computer models simulating the response of the swine and human brain to blast. Equipment required to perform these tests have been ordered and with the exception of the intracranial pressure transducers, all other equipment has been received and tested. The manufacturer of the pressure transducers promised delivery of the equipment in late August 2013 and testing is scheduled to begin in October 2013. A test readiness run is scheduled for July 2013 to ensure all equipment will work as expected and that the test protocol is feasible

15. SUBJECT TERMS
Keywords: Blast-related brain injury, Open field testing of swine and PMHS, Computer modeling of swine and human brain, brain injury mechanisms

16. SECURITY CLASSIFICATION OF:			17. LIMITATION OF ABSTRACT	18. NUMBER OF PAGES	19a. NAME OF RESPONSIBLE PERSON
a. REPORT	b. ABSTRACT	c. THIS PAGE			USAMRMC
U	U	U	UU	50	19b. TELEPHONE NUMBER *(include area code)*

TABLE OF CONTENTS

INTRODUCTION

This research project is designed to determine the cause of mild traumatic brain injury due to blast overpressure and, if possible, the human tolerance to blast overpressure. It consists of an experimental portion in which 12 swine and 6 post-mortem human subjects (PMHS) will be exposed to blast. The experimental effort will be supplemented by a computer modeling section which can extend the results of the tests to blast scenarios not easily achievable experimentally. In this first report, preparatory work for the proposed experiments is described along with the formulation of models of the human and swine brain subjected to blast. Progress in the modeling effort is on schedule but animal and PMHS testing have not begun because of the difficulty in obtaining the intracranial pressure sensors needed to conduct the tests.

STATEMENT OF WORK

The Statement of Work (SOW) for this project is as follows:

I. Perform open field blast testing on 6 anesthetized minipigs to obtain biomechanical data and on 12 anesthetized minipigs to obtain pathohistological data
II. Perform open field blast testing on 6 unembalmed post-mortem human subjects (PMHS) also known as cadavers to obtain biomechanical data
III. Develop and validate a computer model of the pig brain simulating the effects of a blast over-pressure
IV. Develop and validate a computer model of the human brain simulating the effects of a blast over-pressure

TASK I REPORT

Task I - Perform open field blast testing on 6 anesthetized minipigs to obtain biomechanical data and on 12 anesthetized minipigs to obtain pathohistological data (Original Proposal)

In this task, there were three separate work items:
1. Adjustment of the Experimental Design and Methodology
2. Preparations for Blast Studies
3. Preparations for Swine Brain Histology

1. Adjustment of the experimental design and methodology

We have justified the use of 6 swine per blast pressure group for histological studies, using newly available data for our revised power analysis. The proposed changes to the work under this task are provided below at no increase in cost to the project:

We originally proposed that 12 anesthetized Yucatan swine were to survive 24 hours after blast and the brains perfused and studied for histological changes related to blast-induced TBI. Six animals were to be exposed to 150 kPa peak overpressure to the front of the head and 6 exposed to 300 kPa overpressure. In the revised study, the proposed

survival time of the 12 animals has been increased from 24 to 72 hours. Over that time period blast effects will be investigated by various serum biomarkers which will also be validated by corresponding histological changes in the brain at the time of 72 hour sacrifice. Serum samples in these 12 animals will be harvested before blast and 6, 24 and 72 hours post blast to assess biomarker levels. These intervals are based on a recent study in which adult Yorkshire pigs were exposed to mild, moderate or severe blast and the temporal changes in biomarker expression were determined at 6, 24 and 72 hours and 2 weeks after blast (Gyorgy et al., 2011). Serum levels of S100B and myelin basic protein (MBP) peaked at 6-24 hours post blast with little difference in expression between 24 hours and 2 weeks after blast. In addition, there was little difference in neurofilament heavy chain (NF-H) expression between 6 and 72 hours after mild to moderate blast exposure (Gyorgy et al., 2011).

In our study, venous blood will be drawn before blast and 6, 24 and 72 hours after blast for biomarker studies. Proposed biomarkers are S100B, neuron specific enolase (NSE), MBP, NF-H, spectrin breakdown product (SBDP), interleukin 6 (IL-6) and heat shock protein 70 (HSP-70). After obtaining serum biomarker levels out to 72 hours post blast, perfused brains will be harvested and processed for histological assessment along with 6 sham animals. As in the original proposal, brain sections will be assessed for axonal injury (silver staining, beta amyloid precursor protein: ß-APP and neurofilament medium chain: NF-M immunostaining), inflammatory changes (microglial and astrocytic proliferation), cellular injury (caspase 3 immunostain, TUNEL, fluoroJ B and H&E staining) and hemorrhages (Prussian blue).

We have also modified this proposed study by adding 6 sham animals. Our power analyses indicate that 6 animals per group will allow sufficient power if we compared the histological findings in the 12 blast TBI animals to sham animals. To estimate the number of swine required at each blast exposure level, we first examined the findings reported by Sajja et al. (2012) who examined neuronal degeneration following blast-induced neurotrauma in a rodent model. Our primary outcome of interest was neurodegeneration as measured by FluoroJade B (FJB). Sajja et al. (2012) reported extremely large effect sizes (Hedges's unbiased d = 1.23 to 5.71) at 24 h and 48 h, respectively, between the blast induced neurotrauma (BINT) and sham groups. The BINT group showed substantially more FJB-positive neurons in the hippocampus (Sajja et al., 2012). Based on these estimated effect sizes, a sample size of 6 in each of groups will have 99% power to detect a mean difference in FJB-positive neurons in the 150 kPa blast group compared to the sham group. We will also compare the 300 kPa blast group with the 150 kPa blast group and anticipate that this study will have sufficient power to detect a difference in positively stained neurons, if there is one. We noted marked group differences in the standard deviations in Sajja et al. (2012), and, thus, our power analysis was based on using a two-group Satterthwaite t-test with a 0.05 two-sided significance level.

2. Preparations for Blast Studies

(a) Development of procedures for installing and sealing pressure transducers

One of the purposes of the current research is to measure intracranial pressure in anesthetized swine during exposure to a blast. Pressure sensor and strain gauge installation methods were also developed and are described below.

One expired adult pig was used to develop techniques for sensor installation and measurement of intracranial pressure (ICP). This practice run was made with a FISO intracranial pressure (ICP) sensor. For the open-field blasts we will use Kulite ICP sensors(XCL-072-100A,) which are currently on order.

Incisions in the scalp at anterior-superior and posterior regions were made to expose the skull. Small holes, 1/4 inch in diameter, were made on the anterior portion of the parietal bone (P) at the midline, and on the occipital bone 1 cm from the midline (Figure 1A). The holes were drilled using a drill bit with a stop collar. The length of drill bit going through the skull was 8 mm for the parietal bone, 15 mm for occipital bone and 10 mm for the frontal bone. A tapered cutting thread was used to make threads in the holes. A 1/4-inch diameter threaded copper hollow fitting, equipped with a threaded cap (Dorman, Colmar, PA) was screwed into each threaded hole. Then a cannula 1/8 inch in diameter was inserted into the brain to guide the FISO pressure sensor into location. The pressure sensor cable passed through a rubber ring in which there was a hole of the same diameter as that of the Kulite pressure sensor cable. The rubber ring was placed between the fitting and its cap. By tightening cap onto the fitting, the hole was sealed by the rubber ring (Figure 1A & B). Two Micro-Measurements 350 ohm rectangular rosette strain gauges, each with three gauges (CEA-06-062UR-350), were affixed to the skull, one at the frontal bone and one at the occipital bone. (Figure 2B) After the strain gauges were attached to the skull, the swine was ready for testing (Figure 4 A & B).

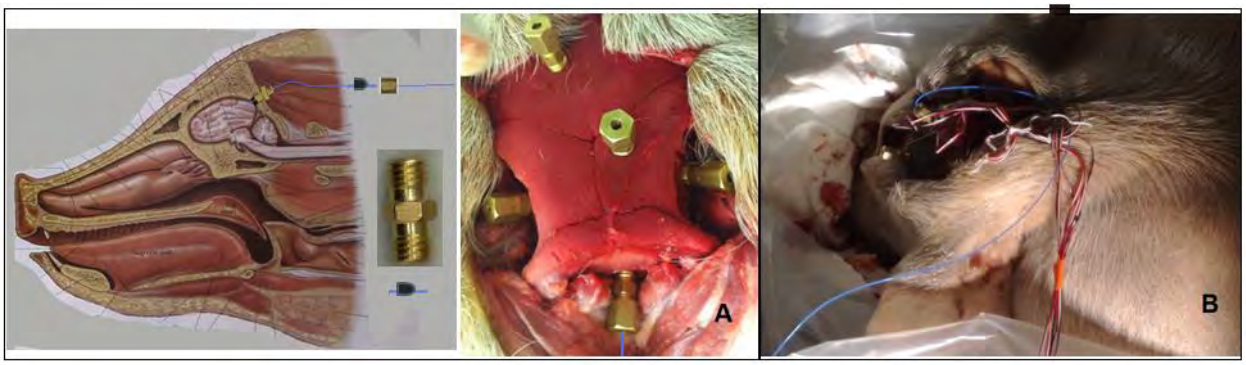

Figure 1. Figure A shows the locations of screws installed. Figure B shows screws installed with the pressure transducers.

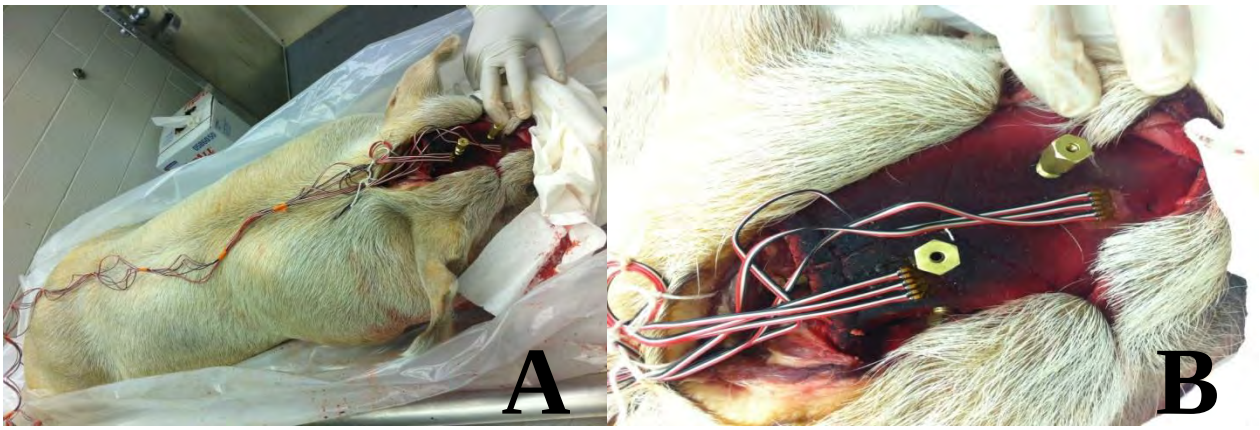

Figure 2. Figure A shows installation of the strain gauges and the pressure transducers. Figure B shows the location of the strain gauges on the skull.

(b) Expired swine blast test using a shock tube

We performed two blast tests with the WSU shock tube on the expired pig described above. The WSU shock tube system consists of a driver chamber and a driven chamber separated by calibrated Mylar membranes. The conical extension was used as shown in Figure 3. The driver, wall and pencil pressure gauges were mounted inside the shock tube to measure the pressure-time histories. FISO ICP data were collected from the frontal lobe in both the tests. The strain gauge data were collected with a TDAS system. Each strain gauge had 3 data channels. The driver pressures were 84.3 and 84.05 kPa respectively in the two tests.

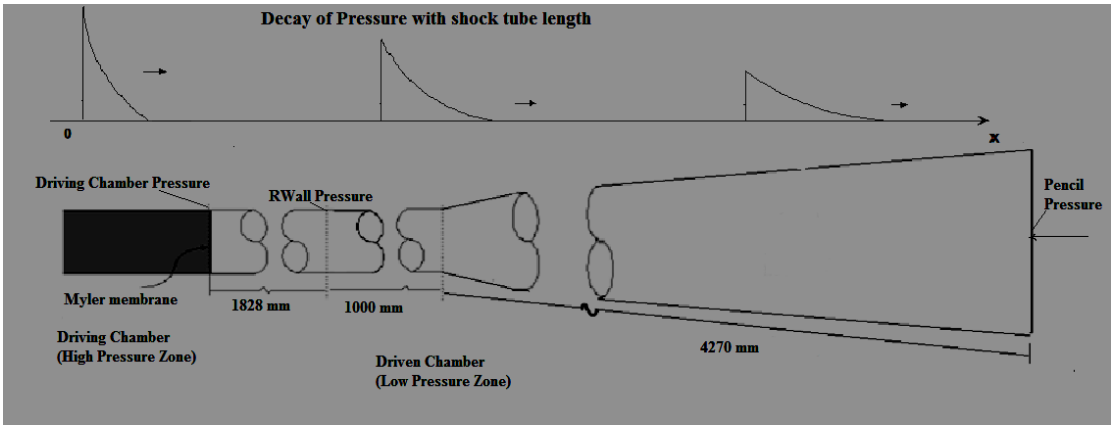

Figure 3: WSU shock tube with a conical extension and pressure gauge locations

Figure 4. Swine shock tube testing setup. Figure A shows data acquisition system with the WSU conical extension in the background. Figure B shows the swine set-up for the swine test blast. The swine cadaver was suspended from a custom-built frame positioned in front of the shock tube.

The results of R wall, driver and FISO (ICP) peak pressures (100 Hz filter) in the two tests are listed in Table 1. The peak unfiltered strains from the six gauges in these two tests are listed in Table 2.

Table 1: Pressure data from the two shock tube tests (psi)

Test 1	R wall	Driver	ICP		**Test 2**	R wall	Driver	ICP
min	-5.75	-6.50	-9.31		Min	-5.97	-6.91	-18.50
max	27.80	84.88	19.94		Max	27.79	84.55	32.15

Table 2: Strain gauge data from the two shock tube tests (Microstrain)

Test 1	1A	1B	1C	2A	2B	2C	**Test 2**	1A	1B	1C	2A	2B	2C
Min	-85	n/a	-77	-43	-131	-366	min	-152	n/a	-457	-264	-91	-364
Max	166	n/a	147	362	281	451	max	173	n/a	249	291	218	253

(c) Configuration of DEWETRON data acquisition system and calibration of sensors

In this period, we purchased a DEWETRON data acquisition system and received training on the usage of this system. The sensors to be connected to the system include strain gauges, linear accelerometers, angular rate sensors and pressure transducers. Five strain gauge rosettes (CAE60-062UR-350/P2,Vishay Precision Group, Inc.) will be used to monitor strain levels at the frontal, occipital, parietal and temporal bones of the skull. The three linear accelerometers (7264D, 2000 g, Meggitt, Inc.) and the three angular rate sensors (ARS-50K-HG, *Diversified Technical Systems*, Inc.) will be fixed to a customized block and mounted to the frontal bone to record 3-D

kinematics of the swine head during blast. Five pressure transducers (Kulite Semiconductor Products, Inc.) will be used to detect pressure changes in designated brain regions. Except for the pressure transducers which are on order, channel setup files for all other individual sensors were created and stored in the DEWETRON control software (DEWESOFT 7.0.1). All channels have been scaled/calibrated. A system set-up file has also been created for future use. The pressure sensors will be connected to the DEWETRON system and configured upon arrival.

(d) Ambulance

A 2006 Ford E450 ambulance was purchased for transport of the anesthetized swine to and from the blast site. The ambulance will be used the next two quarters for transport of sham swine used for baseline histology in this project. The blast site is in Port Clinton, OH at the facilities of ARES, Inc. It is approximately 180 miles from the Wayne State University campus. The test site is approximately 100 ft (30 m) square with a concrete ground surface.

(e) Other Test Equipment

Other test equipment needed for the tests include linear accelerometers, angular rate sensors, high speed cameras, a mobile gantry suspension system for the swine (and PMHS) and miscellaneous equipment to protect the cameras and data acquisition system. Plans for the use of these pieces of equipment with the remote control computer and the pressure sensors can be found under the Task II Report.

(f) Protocol for Open Field Testing of Swine

Six of the 18 swine to be exposed to blast overpressure will be instrumented with pressure sensors, skull strain gauges, accelerometers and angular rate sensors. The method for inserting pressure sensors is described above. The test protocol is described below under Task II Report, Protocol for Open Field Testing of PMHS and Swine.

3. Preparations for Swine Brain Histology

During the past year, various histological techniques have been developed in anticipation of the need to process and perform microscopic studies associate with swine blast studies.

(a) Development of a swine perfusion and brain fixation technique

Based on our pilot perfusion technique using 2 Yucatan pigs and 1 domestic pig, the following perfusion technique has been developed. For this purpose, at the conclusion of their respective survival period, adult male Yucatan mini pigs (50-60 kg) will be euthanized by sodium pentobarbital (fatal plus) followed by rapid opening of chest by a midline sternotomy exposing the heart and major vessels. The sternotomy will be extended to the neck to visualize the trachea and bilateral carotid arteries. Then, a canula will be inserted into each of the carotid arteries and the pig will be flushed with 2

liters of 0.9% sodium chloride solution. The descending aorta, bilateral subclavian and brachial arteries will be clamped (a similar approach was used by Fritz et al, 2005). The right atrium will be opened and the returning blood and solution will be collected directly by suction in to a container for later disposal.

Once the returned solution is clear, the brain will be fixed by 6 liters of 4% paraformaldehyde solution, as described by Browne et al (2011). Then, the skull will be opened and brain will be removed and post fixed in 4% paraformaldehyde (500 ml) to await further processing.

(b) Swine brain processing for histological studies

The cerebral hemispheres and the isolated cerebellum will be cut into 5 mm thick blocks (others used 2 mm blocks[2]) using a pig brain slicer. These blocks will be post fixed in 4% paraformaldehyde with 20% sucrose. Then alternating blocks encompassing the rostral caudal regions will be chosen. These chosen blocks will be placed in equal volume of Tissue-Tek® optimum cutting compound and 20% sucrose (w/v) and frozen in a stream of liquid nitrogen (Saljo et al, 2008). The frozen blocks will be cut into 25-40 µm thick sections on a cryostat (Leica CM3050Leica Microsystems, Heidelberg, Germany) by placing them on a wider diameter specimen disc (part # 14037008637, Leica Microsystems, Heidelberg, Germany). 25 sections from the face of each block will be collected and placed in PBS and 0.1% sodium azide filled multiwall plates (Catalog #462424, Brain Research Laboratories Newton, MA 02468) for later immunocytochemistry procedures. For long-term storage unused sections will be stored in a cryoprotectant solution (25% ethylene glycol, 25% glycerol in 0.1M PB) and stored at -20^{o}C (Saljo, 2008).

(c) Development of a prototype swine brain slicer

Considering that a perfusion technique has been developed and a sectioning technique has been proposed, a validation of the sectioning technique is underway. As part of this validation, first a paraffin mold of the Yucatan mini pig brain was generated. This mold has given further impetus to the generation of a more precise brain mold of the Yucatan swine brain. Using the paraffin brain mold (Figure 1A") developed previously, a prototype brain slicer matrix for Yucatan swine brain was developed (Figure 1A) using pottery clay. This prototype brain matrix has been designed to acquire approximately 5mm thick blocks of brain (Figure 1A') This prototype slicer will enable us to acquire blocks of brain tissue at known anatomical locations for further sectioning (40 µm thick serial sections). These sections will be used in the development and evaluation of various staining techniques to assess neuronal injury, inflammation, and brain hemorrhage after blast. Future plans include development of a machined brain slicer matrix utilizing hard plastic or metal.

Figure 1. Prototype brain slicer modeled after a previous prototype (Figure 1A")

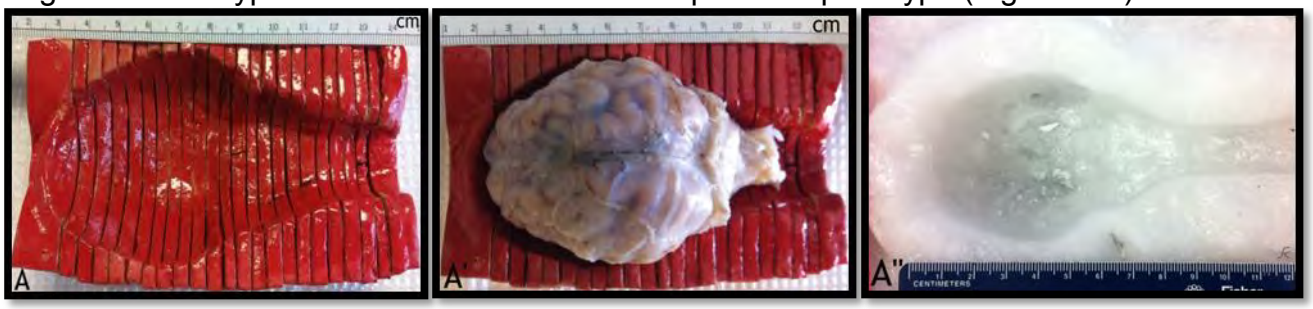

(d) Development of Neurofilament light chain (NF-L) staining to visualize axonal injury

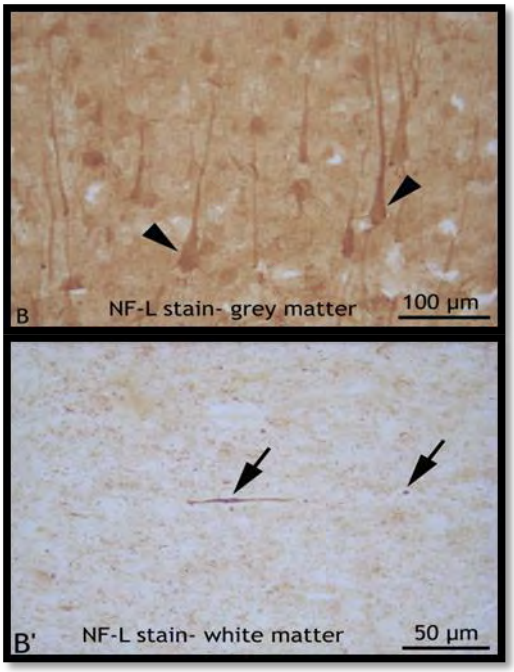

Figure 2.NF-L Staining for axonal injury.

A forebrain block, approximately 5 mm in thickness, from a control Yucatan swine brain was previously cut (using the swine brain matrix prototype A" shown above). This block was further cut into 40 µm thick sections (Leica CM3050Leica Microsystems, Heidelberg, Germany) that were collected in a large multiwell box filled with PBS and 0.1% sodium azide. Representative sections were processed for neurofilament light (NF-L) chain immunohistochemistry (IHC). The sections were briefly boiled in citrate buffer solution in microwave and then incubated in the same citrate buffer solution (90 min at 90^{o}C). The sections were then incubated overnight in rabbit NF-L antibody (1:1000; cat # AB 9568, Millipore, Temecula, CA 92590) and then developed by avidin biotin peroxidase reactivity. Further observation of these sections under light microscope revealed well stained cell bodies (Fig. 2B) with their apical dendrites as well as stained axons in the white matter tract (Figure 2B'). These preliminary observations support the potential of using NF-L IHC in assessing axonal injury changes following blast exposure.

(e) Development of Glial Fibrillary Acidic Protein (GFAP) staining

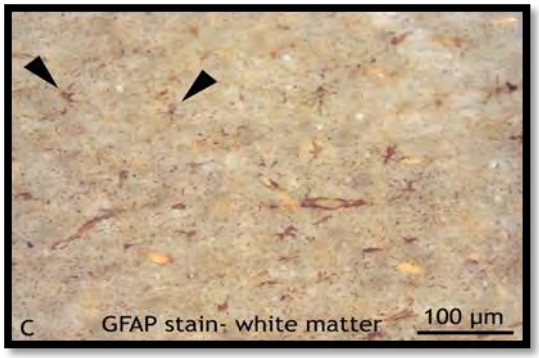

Figure 3. GFAP Staining in white

Representative swine brain sections were also assessed for the presence of astrocytes using the citrate buffer antigen retrieval method described above. The sections were incubated overnight in a mouse anti GFAP cocktail (1:1000; cat # NE1015, Calbiochem), and then developed by avidin biotin peroxidase reactivity. Observation of these sections under light microscope revealed well stained astrocytes (Figure 3) in both white and grey matter regions. In the sections observed, there matter appeared to be a preponderance of astrocytes in the white matter compared to those in the grey matter.

(f) Ongoing work related to development of other staining techniques

Currently we are also focused on developing a Nissal staining technique that will help visualize cellular injury changes in sham and blast exposed swine brains in conjunction with various other staining techniques as proposed in this study. Effort is also directed at developing a reliable silver staining method to visualize axonal injury in various regions of the swine brain. The silver staining will complement axonal injury changes as evidenced by NF-L and β-APP staining. Although we have extensive experience in using β-APP staining technique in studies related to traumatic brain injury (Li et al, 2011 and Kallakuri et al, 2012), we are currently working on optimizing the technique for swine brain.

TASK II REPORT

Task 2 - Perform open field blast testing on 6 unembalmed post-mortem human subjects (PMHS) also known as cadavers to obtain biomechanical data.

1. Acquisition of Test Equipment

A large portion of time was spent on acquiring quotes and performing research to obtain the equipment most capable of capturing porcine and PMHS response under primary blast loading conditions. The items listed below have been acquired and are shown in Figures 4 through 11:

- Endevco 7264D linear accelerometers
- Vishay CEA-06-062UR-350 rosette-style strain gages
- DTS ARS HG angular rate sensors
- NAC Memrecam HX-3 and GX-8 digital high speed cameras
- Dewetron 3050 DAQ data acquisition system
- NETGEAR 8 port gigabit hub switch
- Two quick-mount low-height manual trolleys
- Two steel hand chain hoists
- A mobile clinic trailer
- APC Smart-UPS RT 1500

(a)

(b)

Figure 4. (a) Endevco 7264D linear accelerometers, and (b) DTS ARS HG angular rate sensors

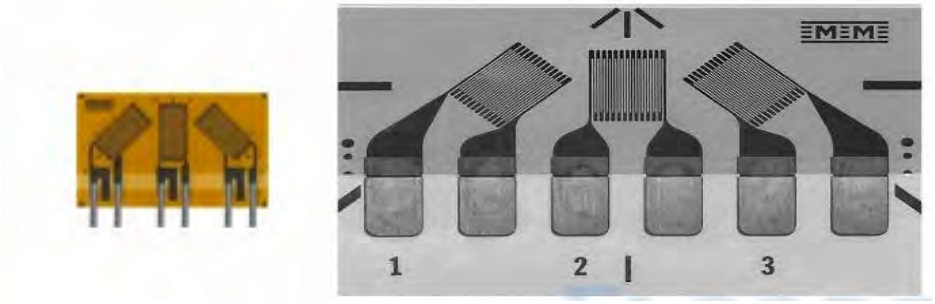

Figure 5. Vishay CEA-06-062UR-350 rosette-style strain gages

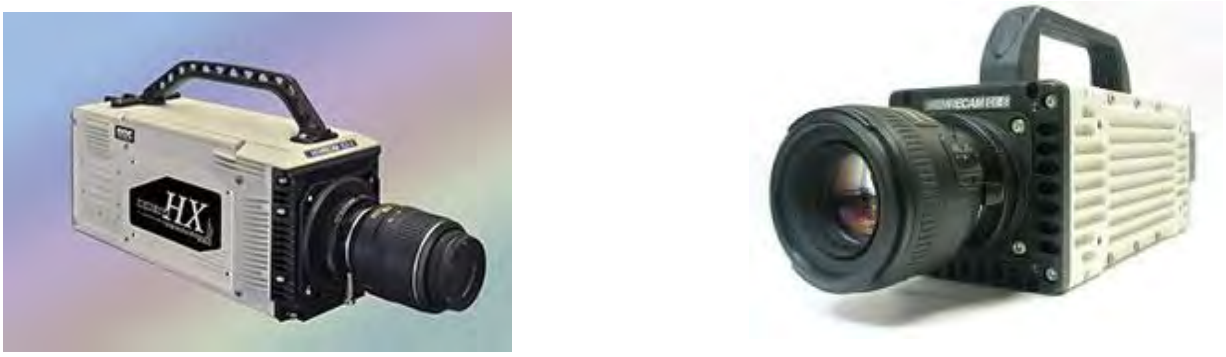

Figure 6. The NAC Memrecam HX-3 and GX-8

Figure 7. Dewetron 3050 DAQ data acquisition system

Figure 8. NETGEAR 8 port gigabit hub switch

(a) (b)

Figure 9. (a) Quick-mount low-height manual trolleys and (b) steel hand chain hoist

Figure 10. The mobile clinic trailer

Figure 11. APC SURTA 1500 XLQ Smart-UPS

The Kulite XCL-072A miniature pressure transducers (Figure 12) have been ordered and their delivery is promised for late August 2013. It is anticipated that they can be made ready for testing in early October 2013. There was a delay in the ordering of these sensors because we needed to determine the advantages of the Kulite piezoelectric sensors versus the FISO optical sensors. The Kulites were more durable but appeared to be only able to measure pressure acting on its sensitive surface (not omnidirectional). The FISO appeared to have omnidirectional capabilities but were not durable and a large number of these sensors needed to be on hand in case of breakage. After it was determined that the FISO sensors were also not omnidirectional, it was decided to order the Kulites.

Figure 12. Kulite XCL-072A miniature pressure probe/surface mount sensor.

2. Integration of Test Equipment

A remote control laptop computer will be used to control the two high speed cameras and the Dewetron 3050 data acquisition system which will record data from the Kulite pressure sensors, the strain guages, the linear accelerometers and the angular rate sensor.

Kulite XCL-072A miniature pressure transducers were chosen to collect intracranial pressure data due to their durability in comparison with the optical FISO sensors and to yield accurate data. For the PMHS experiments, it is of prime importance that we use freshly dead unembalmed cadavers and that we pressurize the cranial cavity just prior

to the blast to obtain an accurate intracranial pressure response. Kulite sensors also have the frequency response to capture the initial rise of the shock wave. However, a reliable method for the installation is necessary to ensure sealing the cavity in the skull so as to maintain the 'typical' CSF pressure. The sealing method was described above, under Task I Report.

The NAC Memrecam HX-3 and the GX-8 high speed cameras, and Dewetron 3050 were successfully linked and controlled by a remote computer via a Netgear hub switch. The gigabit switch is also used to support data transferring between the high-speed cameras and the laptop. This "remote LAN control" setup enables the immediate and complete control on the data acquisition instrumentation (cameras and Dewetron) that will be positioned outside the blast zone, ensuring the ability to change setups of the data acquisition instrumentation and monitor their real-time conditions at a safe distance. Laboratory tests have been conducted on angular and linear sensors in addition to recording video data. Before the first on-site test readiness run (TRR) scheduled for July 2013, proper lenses, tripods, and instrumentation protection will be acquired and prepared for testing.

3. Mobile Gantry to Suspend Test Subjects

A mobile 10-ft long gantry with an A-frame has been designed and fabricated to securely hang both the PMHS and swine subjects via the available trolleys and manual chain hoists. A 360º hook will facilitate rotation of the test subjects (PMHS/pig). The gantry has been designed to provide adequate control on the height and pressure impact direction of the subject's head and yet it is flexible and large enough to accommodate both the swine and PMHS. A harness was improvised to hold the test subject securely in an inverted position. To demonstrate the lifting capability of the gantry, an automotive crash dummy was hung upside down facing three directions as proposed (Figure 13).

Figure 13. A 5th percentile female dummy hanging securely in three different orientations on the mobile A-frame gantry.

4. Temporary PMHS Laboratory:

A Turtle Top mobile clinic trailer will be used as a temporary PMHS lab while we are on site in Ohio. The trailer was delivered in May 2013 (Figure 10). The trailer has been inspected for travel readiness. A proper hitch and ball mount was attached to a Ford F-

150 pickup truck that will be used to tow the trailer. The trailer is equipped with a mobile autopsy table, refrigerated space for PMHS storage, containers for water and an AC 7000-watt generator to operate coolers and lights. There are four trays for PHMS test subjects.

A separate portable Honda inverter generator will be used on site to power our high speed cameras and the Dewetron 3050 data acquisition system. An APC SURTA 1500 XLQ Smart-UPS will ensure that the power to the instrumentation and cameras is clean and stable.

The clinical equipment, water system, heater, clinic, A/C, refrigerator is being tested using the onboard mobile generator to insure field trip readiness. A test readiness run (TRR) will be carried out in July 2013 to ensure that all equipment are functioning properly and that we can acquire the needed data at the ARES test site in Ohio.

5. Protocol for Open Field Testing of PMHS and Swine

- A total of six instrumented whole PMHS (and swine) will be exposed to open field blasts in accordance with the project plan of work. Each test subject will undergo nine tests per day to acquire field blast data at three pressure levels (150, 300, and 450 kPa) and facing three directions (frontal, lateral, and occipital).
- Pressure Transducers (Kulite XCL-072A miniature pressure probe) will be inserted using skull trephines in the frontal, temporal, parietal, occipital lobes.
- X-rays will be taken from two different directions of the test subject's head so that exact 3D coordinates of the pressures transducers locations can be established.
- Seven rectangular Rosette strain gauges (Vishay CEA-06-062UR-350)will be attached to the cranium , one at each of the following bones: frontal , mandible, zygoma , sphenoid , temporal , parietal , and occipital . Gauges will be placed on one side of the head only because symmetry is assumed for frontal and occipital exposures.
- Additional gauges may be applied to the skull if the head modeling study predicts possible sites for large skull deformations due to blast over pressure.
- A light weight 6-degrees of freedom sensor package will be mounted at midline near the vertex of the skull to assess the linear acceleration and angular velocity of the head. (Endevco 7264D linear accelerometers and DTS ARS HG sensors)
- Instrumentation will be installed at WSU; the mobile clinical trailer (and ambulance) will facilitate and provide an adequate environment to complete all necessary remedial work during the blast test (e.g. broken wire, dislocated sensors, etc.).
- PMHS will be delivered to Ohio by a licensed transportation company. A specially designed mobile clinic (Turtle top trailer) will be used to transport the PMHS to the proving ground, making use of the specially designed refrigerator annex. As stated in Task I Report, above, the swine will be transported in the ambulance on the day of the test.

- A portable Honda inverter generator and an APC Surta 1500 XLQ will be used to provide stable and continuous power for all on-site test instrumentation throughout the field test duration.
- PMHS will be held upside down with the help of a mobile A-Frame Gantry, a manual sling, a trolley, and an improvised body harness. This arrangement will help to get rid of the air bubbles, which were likely introduced into the skull during installing pressure sensors. The swine will be placed in sling with four holes for their extremities.
- The height and distance between head of the test subject and the charge will be determined through some trial tests using a Hybrid III dummy.
- The test subject will be constraint from excessive motion during the blast.
- Pressure readings will be recorded at 250 kHz, and acceleration, angular velocity, and strain data will be collected at 20 kHz, using the Dewetron 3050 data acquisition system.
- NAC Memrecam HX-3 and GX-8 digital high speed cameras will be used to record the overall kinematics at 10000 fps.
- Intracranial pressures will be displayed as a function of time for each of the sensors and correlated with the time of the initiation of the blast wave.
- Statistical analysis will be conducted to establish the strain corridors for different cranial bones as a function of blast severity.
- Wave transmission speed and mechanical properties of the cranium due to high rate loading will be established.
- The relationships between the wave transmission through the skull and its effect on the intracranial pressure will be established.
- Corridors of the intracranial pressure will be established as a function of blast severity for model validation.

TASK III Report

Task III - Develop and validate a computer model of the pig brain simulating the effects of a blast over-pressure

In this reporting period, we can report on the following four aspects of work related to pig head modeling:

1. Literature review of current models of the pig head under air blast loading
2. Development of a 2-D pig head FE model to study the influence of cerebrospinal fluid (CSF) on the shock wave response
3. Development of the geometric model for the head of a 55-kg Yucatan pig
4. Performance of blast simulations to study the effect of PMHS test fixtures on the wave reflection.

1. Literature review of current models of the pig head under air blast loading

In recent years, a number of numerical models have been developed to study the biomechanical response of the head under shock wave loading. As pointed out by Yang et al. (2010), most of the modeling work is focused on the human head. However, these models were largely insufficiently validated against experimental data. On the contrary, animal head models, especially large animals such as pig, are not as well studied. In this report, two computational modeling studies on the pig head are summarized.

Teland et al. (2010 a, b) experimentally and numerically investigated the blast effects from weapons on the brain of a simulated operator (pig). The sources of the shock wave came from two weapons used by the Swedish Army, namely, an AG90, a 12.7 mm anti-materiel rifle (Barret Firearms Manufacturing, Mufreesboro, TN, USA), and a FH77, 155 mm howitzer (SAAB Bofors 8 Dynamics AB, Sweden). Anesthetized pigs were placed in the gunner's position and received 3 consecutive exposures, as shown in Figure 14. The pressure-time curves inside the pig brain and outside the pig head were recorded with hydrophones (diam. 9.5 mm, model 8100; Bruel&Kjar).

Figure 14. Position of pigs in animal experiments (FH77 to the left, AG90 to the right)

An explicit hydrocode, AUTODYNA, was used to simulate the shock wave loading events with an arbitrary Lagrangian–Eulerian (ALE) algorithm. The pressure wave generated from the relevant weapons was approximated with numerical blast waves from spherical detonations of TNT charge. The mass and standoff distance of the charge were estimated with a trial-and-error approach. It should be noted that this is an approximate method, since no charge was used in the tests. The pig head model geometry was highly simplified and consisted of only two materials: skull bone and brain, as shown in Figure 15a. A cross-sectional view of the actual pig head is shown in Figure 15b for comparison purposes. Both the skull and brain were assumed to behave elastically. A fairly good agreement was obtained between the experiment and prediction of incoming pressure waves. No comparison of intracranial pressures was reported in this paper.

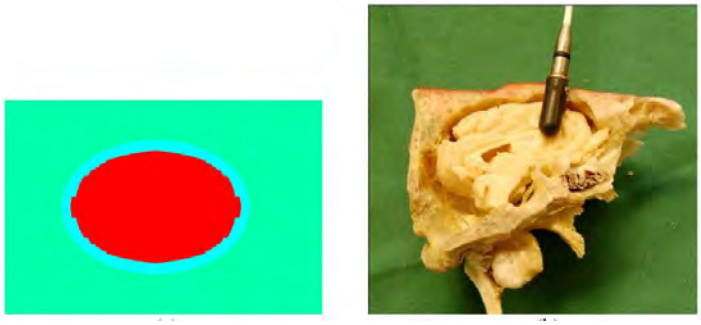

(a) (b)

Figure 15. (a) FE model of the pig head (Teland et al, 2010a, b); (b) Cross section of the actual pig head

More recently, Zhu et al. (2013) performed a study on the biomechanical responses of the pig head under a specific shock tube environment based on the results from a Small Business Innovation Research (SBIR) project. A finite element model of the head of a 50-kg Yorkshire pig was developed with sufficient details as shown in Figure 16. The mesh was built using the software package HYPERMESH 11.0 (Altair, Troy, MI) and CFD/HEXA 12.0 (ANSYS, Canonsburg, PA) based on computed tomography (CT) and MRI images of a pig head. The pig was of the same type and was similar in weight to the specimens tested. The principal features of the head such as the skull, brain, CSF, dura, and pia were modeled. The average mesh size of the FE model was 1 mm and the whole model consisted of 1,217,420 hexahedral elements with one-point reduced integration formulation. The material properties of pig skull and brain tissues were taken from the published literature (Wood 1971; Arbogast et al. 1997; Tamura et al. 2007).

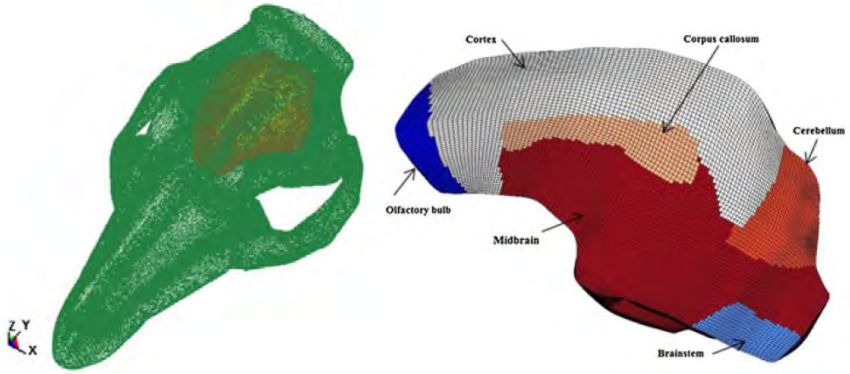

(a) (b)

Figure 16. Pig head FE model (Zhu et al, 2013): (a) skull and brain and (b) partition of the brain (enlarged view).

The shock tube model was developed using the multimaterial arbitrary Lagrangian–Eulerian (MMALE) approach. These two models were integrated and a fluid/solid coupling algorithm was used to simulate the interaction of the shock wave with the pig's head. The model setup is shown in Figure 17. The finite element model-predicted incident and intracranial pressure traces were in reasonable agreement with those obtained experimentally. Further examination of the verified numerical model of the shock tube and pig head revealed that the distributions of pressure, shear stress, and principal strain within the head were dramatically different throughout. Pressure

enhancement, caused by shock wave reflection at the interface of the materials with distinct differences in wave impedance, was found in the skull as seen in Figure 17. Brain tissue has a shock attenuation effect and larger pressures were observed at the frontal and occipital regions, suggesting a greater possibility of coup and contrecoup injuries. Shear stresses in the brain and deflection in the skull remained at a low level. Higher principal strains were observed near the foramen magnum, indicating a greater chance of cellular or vascular injuries in the brainstem area.

2. Development of a 2-D pig head FE model to study the influence of CSF on the shock wave response

A recent experimental study (de Lanerolle et al. 2011) on the blast-loaded pig head indicates that the blast pressures of 35±11 psi can cause axonal injury at the boundary of ventricle and brain tissue as shown in Figure 18. The injury was detected by β-amyloid precursor protein immunohistochemistry.

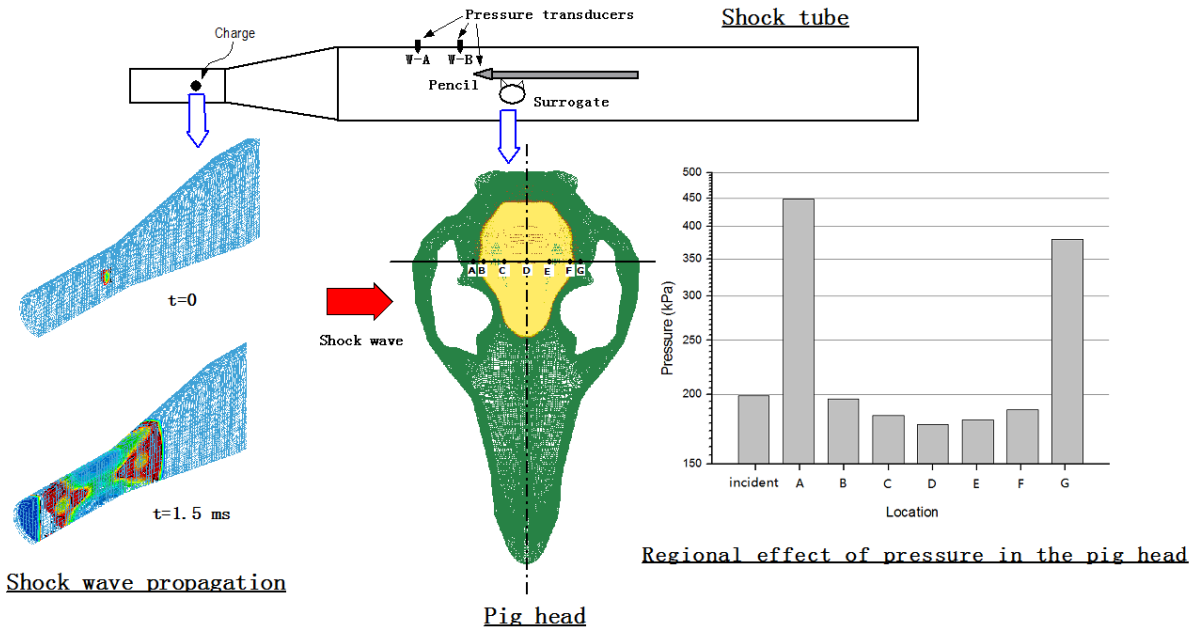

Figure 17. Numerical modeling setup of a pig head in a shock tube environment. Regional effect of peak intracranial pressure (ICP) is also shown.

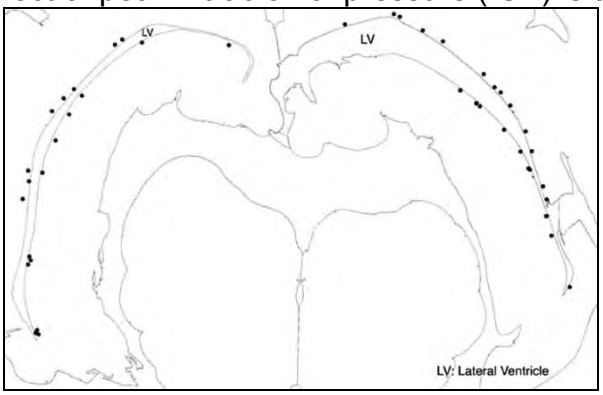

Figure 18. Locations of axonal injury identified by the dark points (de Lanerolle et al. 2011)

To study the possible effect of blast overpressure on the ventricle, a 2-D pig head model was developed based on a 3D digital pig brain atlas (Sikali et al. 2010). The 2-D model was used because it was able to study the points of interest (POI) in the brain in detail while not significantly increasing computational time if a 3D mode were used. Although the species of the pig head in the atlas is different with that of the pig to be tested, the results are still informative and the basic trends can be obtained. A coronal slice taken from the atlas is shown in Figure 19(a), which was similar in location as that shown in Figure 18. The geometric model was then converted to an FE mesh with an average element size of 1.5 mm, and a simplified skull was added as illustrated in Figure 19(b). The shock wave was assumed to come towards the right side of the head.

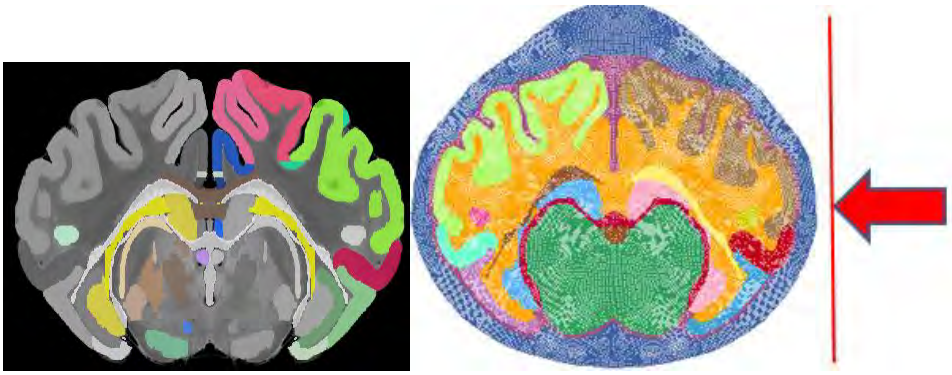

(a) (b)

Figure 19. (a) A coronal view of a pig brain; (b) A 2D FE model developed based on the gometric model in (a)

The model was constrained in the out-of-plane direction and free to deform and move in the in-plane directions. The material properties of skull and brain were identical to those used by Zhu et al. (2013). The CSF was modeled as an elastic fluid, with a very low Young's modulus (0.1 kPa) and very high Poisson's ratio (0.499). Bulk modulus was 2.19 GPa which is the same as that of other brain tissues. The shock waves were simplified as a triangular pressure wave with a constant duration of 5 ms. The peak pressures were in the range of 50 to 400 kPa with an interval of 50 kPa. The predicted ICP peaks, maximum shear strain, and strain rate at the CSF and brain tissue are given in Table 3. It can be seen that the ICP peaks are similar in both the ventricle and the brain. The maximum strain and strain rate in the ventricle are about 5 times and 9 tiimes higher than those in the brain tissue, respectively. Therefore one may conclude that the fluid in the ventricle has little influence on the pressure but can signifcantly influence the strain/strain rate of the brain tissue. It should be noted that due to the 2-D boundary conditions, the predicted results are largely qualitive with the emphasis placed on the trend, rather than exact values.

Table 3. Simulation results using the 2D model

Peak incident pressure (kPa)	Peak ICP* (kPa) – Coup site		Maximum shear strain (%)		Maximum strain rate (/s)	
	CSF	Brain tissue	CSF	Brain tissue	CSF	Brain tissue
50	262	254	3.7	0.6	41	4.3
100	525	509	7.6	1.1	58	7.5
200	1049	1017	15.4	2.3	151	17.1
300	3674	3309	23.3	3.4	254	26.8
400	4971	4481	32.6	4.6	311	35.9

Typical pressue contours at 1 ms and maximum shear strain at 6 ms at the incident pressue level of 200 kPa are shown in Figures 20(a) and 20(b), respectively. It can be seen that the ICP has a gradient pattern throughout the brain. The magnitude of peak pressure is determined by the distance from the blast source and is irrelevent to the regions with CSF. Shear strain, on the othe hand, is much higher in the fluid filled regions because of the much lower stiffness of the CSF. The relationship between the axonal injury and material properties will be studied in more detail in the future. Although the maximum strain is still relatively low, Figure 20(b) highlights the resemblance in location between the strain map and the injury map shown in Figure 18.

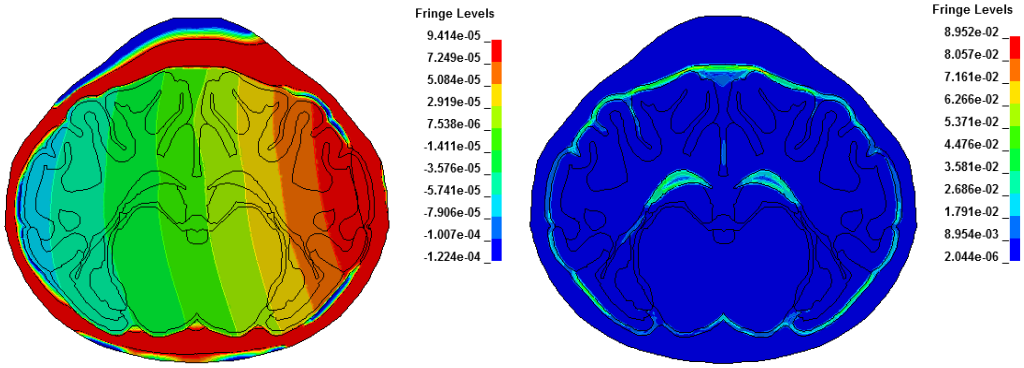

(a) (b)

Figure 20: Regional effect of (a) ICP and (b) maximum shear strain at the incident pressure level of 200 kPa

3. Development of a geometric model of the head of a 55-kg Yucatan pig

MRI images of the head of a 55-kg Yucatan pig were obtained and are shown in Figure 21. The image resolution was 0.6 by 0.6 by 1.0 mm. The data processing procedures consisted of the following steps: image registration, image processing, generation of the 3-D geometry of the head, 3-D geometric shaping, and finite element mesh development.

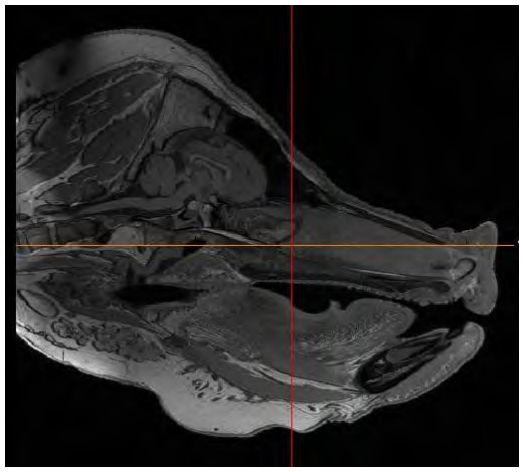

Figure 21. A sagittal MRI image of the Yucatan pig head

The images were imported into MIMICS (Materialise, Leuven, Belgium) for co-registration in order to translate the images from different modalities into the same global coordinate system. Upon completion of co-registration, image processing could commence, and the geometries of interest were isolated through a combination of thresholding techniques. Thresholding allows the user to isolate a certain density, for example, bone or soft tissue, using image pixel values (intensity). This process was conducted in MIMICS, using objects called “masks.” These masks are essentially organizational tools to help isolate bone from other tissues, for example. An example of the application of a mask is shown in Figure 22.

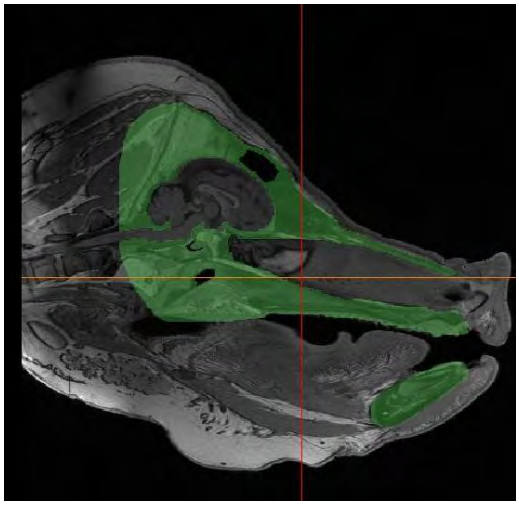

Figure 22. A sagittal MRI view of thresholding example for the pig skull

This operation was repeated layer by layer until the 3-D geometry of the whole head was obtained. Then the geometric model can be exported in NASTRAIN format which includes the surface information as shown in Figure 23, where skull, brain and spinal cord are marked with different colors.

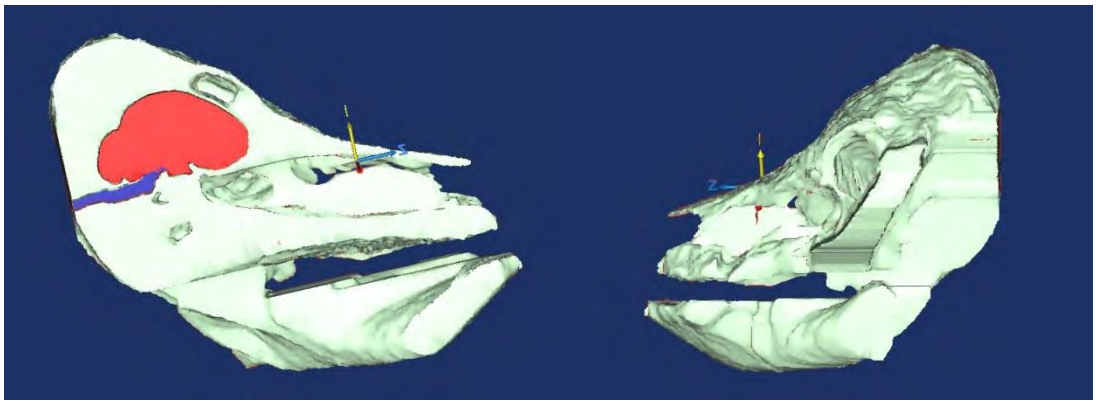

Figure 23. Geometric model of the pig head

Once the intial geometric modeling was finished, a re-shaping technqiue was used to ensure that the model surface could meet strict meshing criteria. Three-dimensional geometric shaping primarily involves the process of smoothing a surface in an effort to create an ideal surface for automated meshing algorithms which use mesh projection-based methods. These methods require avoiding very sharp surfaces or very small holes. Such geometric features do not have much influence on the simulation results but can incrase the compuational time significantly. Figure 24 shows the geometric model after re-shaping.

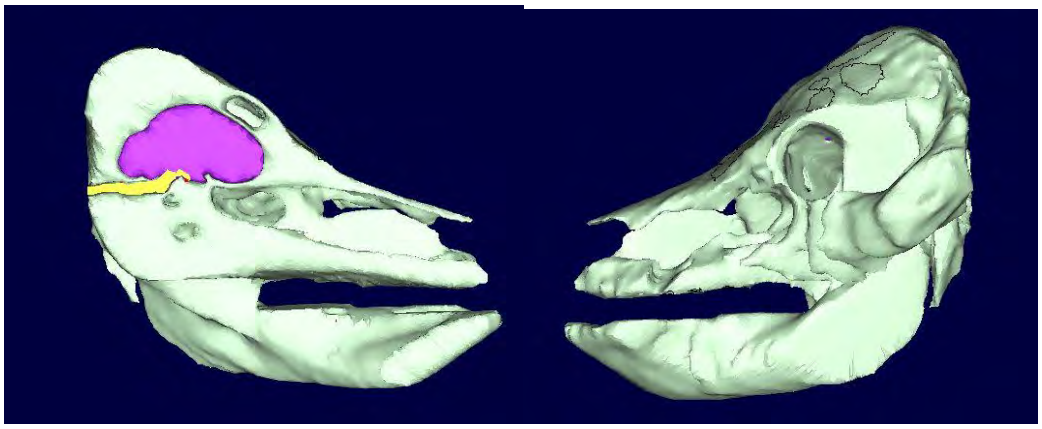

Figure 24. The geometric model after re-shaping

Then the pig head geometric model was converted into an FE mesh. Two pig head FE models were built with different types of elements, i.e. tetrahedral and hexahedral elements respectively, to describe the pig skull. In both cases, the brain part was modeled with a hexahedral mesh, and the nodes at the skull/brain interface were connected.

Pig head model with a tetrahedral mesh for the skull

Figure 25 shows the pig head model with a tetrahedral mesh for the skull. Meshing an object using tetrahedral elements is straightforward and it can be implemented automatically using commercial meshing tools such as Hypermesh. This is the fastest way to develop an FE model with a rather complicated profile. However, in FE simulations, the tetrahedral mesh tends to increase the material stiffness, particularly

when the deformation is large. To this end, this model will only be used for preliminary simulations to debug the blast loading conditions.

Figure 25. The pig head model with a tetrahedral mesh for the skull: (Left) Outside profile; (Right) Mid-sagittal view

Pig head model with a hexahedral mesh for the skull

The hexahedral FE mesh was developed using ANSYS ICEM (ANSYS Inc. Canonsburg, PA), a pre-processor based on a multi-block meshing scheme aimed at hexahedral mesh generation. The multi-block technique (Shivanna et al. 2010) is based on rules for geometrical grid-subdivisions (i.e. 'blocks') and mapping techniques; producing hexahedral elements in three-dimensional (3-D) space. The structured grids have a regular topology where the neighborhood relation between all points is captured within a three-dimensional array. This is an emerging robust method which can reduce computational cost and produce a higher quality hexahedral mesh than conventional meshing techniques. In the modeling work, a new mesh was first built for the brain that could be projected to the skull surface. Blocks were fitted into the brain geometry as shown in Figure 26.

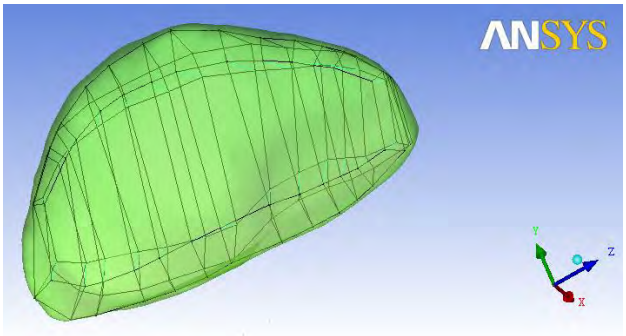

Figure 26. The created brain blocks

After the blocks were established, the 'pre-mesh' function was applied to create the mesh with the specified element size, that is, 1-2 mm in the current case. The result was a high quality hexahedral mesh, as shown in Figure 27.

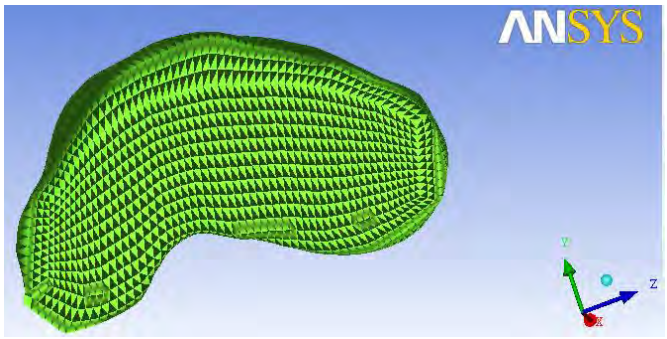

Figure 27. The created brain mesh

The pig skull model was created based on this brain model. It was implemented by projecting the elements of the brain exterior to the surface of the skull, as shown in Figure 28. Using the nodal locations on the brain mesh as a “source geometry” and the skull as the “destination geometry,” a linear mesh generation function in the Hyperworks software package was applied to create the final hexahedral mesh. The linear mesh generation function requires that the source and destination surface geometries have the exact same number of elements. Projecting the elements node-by-node from the surface of the brain to the surface of the skull ensured that the element count, on each surface, would remain the same. However, due to the complexity of the geometry of the pig skull, the elements could only be projected in a local region around the brain, as seen in Figure 28. The generated mesh of the skull is shown in Figure 29.

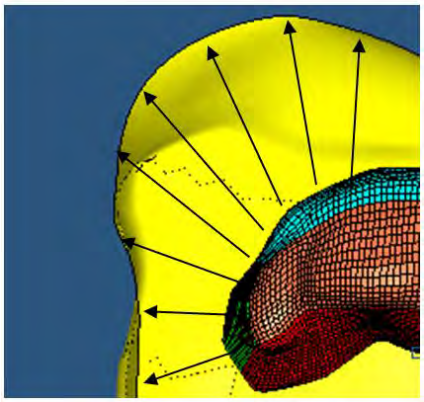

Figure 28. Element projection scheme for the skull mesh generation

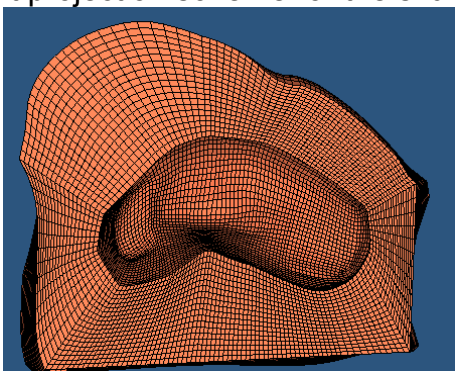

Figure 29. The generated hexahedral mesh for the local part of the skull

The newly created mesh in the local region of skull (i.e. Figure 29) was then used as a template for extracting the mesh for the rest of the skull. This was completed by first creating the 2-D mesh at the external boundary of the facial bones. Each 2-D mesh slice was copied from the previous mesh, to ensure that the number of elements would remain the same to allow use of the same linear mesh generation feature to create the solid skull mesh, as illustrated in Figure 30. The sagittal view of skull mesh can be seen in Figure 31.

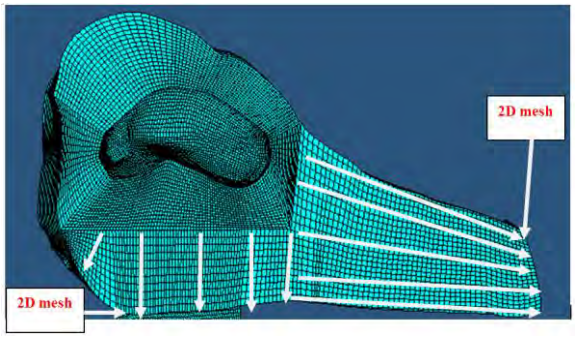

Figure 30. Extract the mesh to the rest of the facial bone

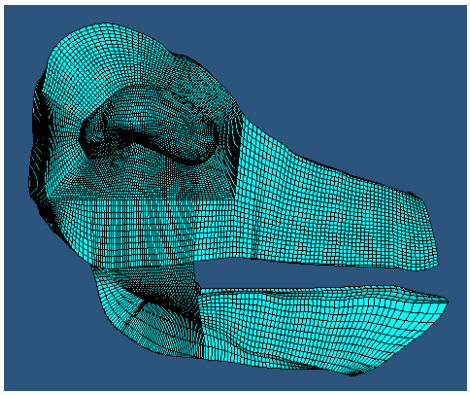
Figure 31. The sagittal view of the whole skull mesh

Using the same method, the mesh for temporal bones was extracted, as shown in Figure 32. The outside view of the whole skull mesh is illustrated in Figure 33.

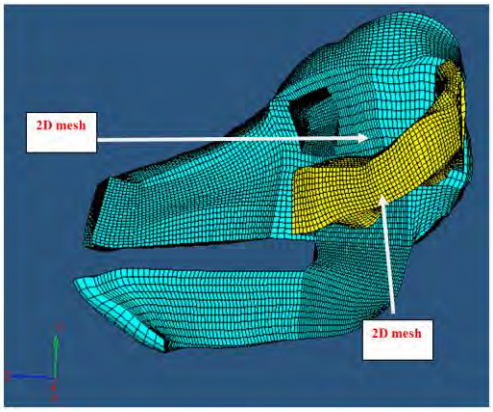

Figure 32. Meshing the temporal bone

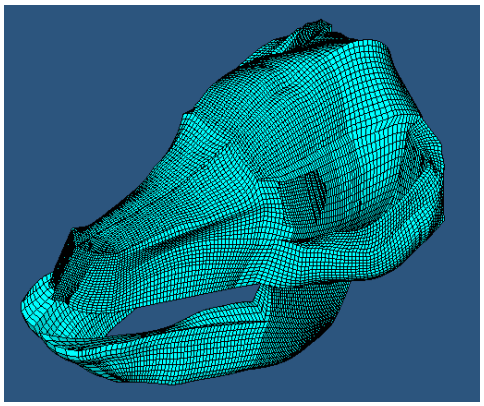

Figure 33. Outside view of the pig head FE model

The 3-D FE pig head model was further refined to improve its bio-fidelity. The outside profile and sagittal cross-sectional view are shown in Figures 34a and b, respectively.

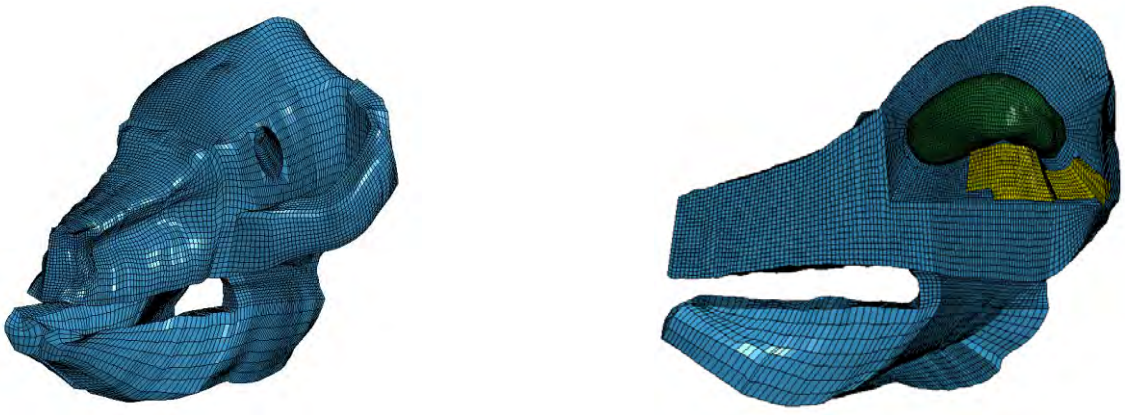

(a) (b)

Figure 34. The pig head FE model: (a) Outside profile; (b) Sagittal cross-sectional view

The whole model consisted of 252,836 hexahedral solid elements. The distribution of Jacobian values, an indicator of mesh quality, is listed in Table 4. Only 1% of the mesh has a Jacobian value of 0.6 or less indicating that the mesh quality was good.

Table 4. Jacobian value of the pig head FE mesh

Jacobian value	[0, 0.6)	[0.6, 0.7)	[0.7, 0.8)	[0.8, 0.9)	[0.9, 1.0]
Percentage	1%	2%	5%	21%	71%

4. Simulation of Wave Reflections due to the Presence of a Test Subject Support Structure

Numerical simulations were conducted to examine the wave reflection effect caused by the structure on which the pig (or PMHS) is mounted. Two simulation techniques used for comparison purposes. They are the CONWEP and multi-material arbitrary-Lagrangian-Eulerian (MMALE) methods. For each approach, two boundary conditions, with and without the fixture, were conducted.

CONWEP simulation

CONWEP is a blast simulation software developed by the US Army in 1991 and it has been integrated into LS-Dyna. The input parameters include equivalent TNT mass, type of blast (surface or air), detonation location, and surface identification where the pressure is applied. A schematic set-up for the CONWEP Simulation is shown in Figure 35.

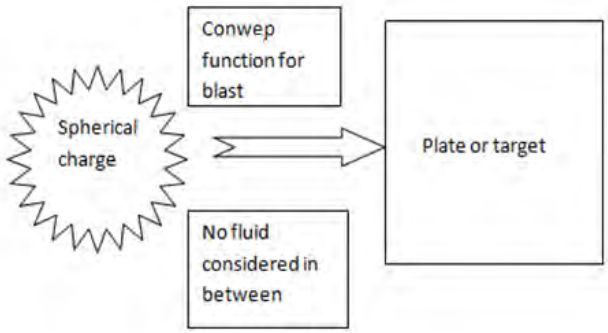

Figure 35. Schematic set-up for CONWEP simulation

The inputs required for *LOAD_BLAST consisted primarily of the explosive equivalent TNT mass, WGT, the location of the center of the charge (XB0,YB0,ZB0) and the time of detonation (burst). An additional parameter, ISURF, allows for the option of a surface (ISURF=1) or free air (ISURF=2) burst. Figure 36 shows the sample input file for 8 lb of TNT equivalent, located at 12 ft, for a free air burst.

The original plan was to place the test subject on a platform (Lift model 512 A). It has a height of 6 ft which can be extended to 12 ft. The fixture consisted of a flat platform that could be moved up or down on a post. A height of 4 ft from the ground was used for the current simulation. The lift and platform were assumed to be made of steel. A simplified pig head and body assembly was modeled and placed on the fixture model. The detonation standoff distance was assumed to be 12 ft and the explosive with a TNT equivalent of 8 lb was used in the current simulation.

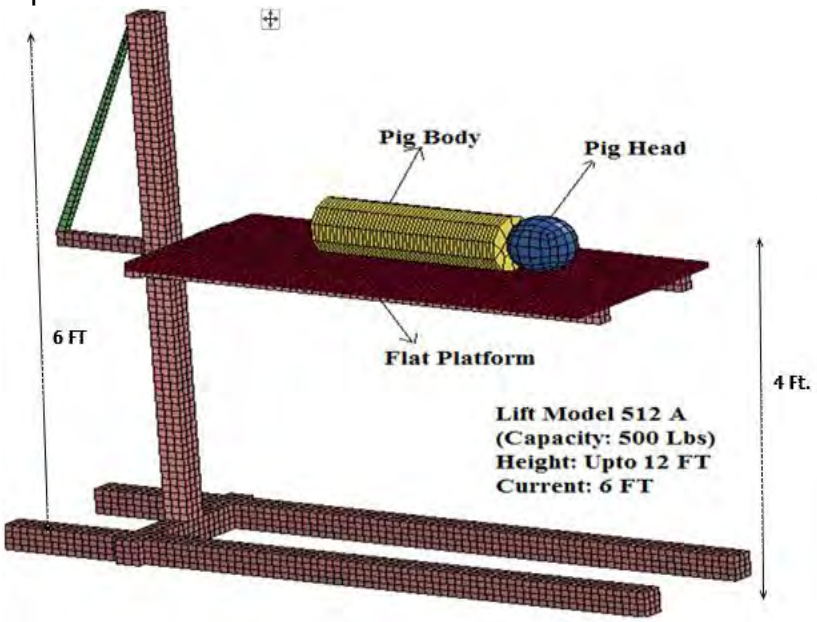

Figure 36. FE model of the simplified pig and fixture

MMALE simulation

Since CONWEP is based on empirical static pressure equations, it does not account for the gas flow produced in the explosion, i.e. dynamic pressure. To eliminate this limitation, the same loading condition was simulated using the MMALE approach. In the new model, the air surrounding the assembly was modeled using eight-noded Eulerian brick elements with a minimum element size of 60 mm, as shown in Figure 37.
Figure 37. Simulation set-up for MMALE case

The explosive was modeled using MAT_HIGH_RXPLOSIVE_BURN card in the LS-Dyna material database together with the JWL EOS. The simulated blast loading events for the case without fixture at the different time points are illustrated in Figure 38, where the generation and propagation of the blast wave are clearly shown.

Results and Discussion

The model predicted pressure–time histories on the frontal, top and left surface of the pig head are plotted in Figures 39a, b and c, respectively.

Figure 39 shows that under current loading conditions, the fixture had no significant influence on the pressure response at the three monitored locations. The finding was confirmed by both the CONWEP and MMALE simulations. The regional effect of pressure has a similar trend, i.e. the highest pressure can be observed on the frontal surface of the head, which is caused by wave reflection. The pressure levels at the left and top locations were about the same. The CONWEP and MMALE predictions have an evident discrepancy in terms of pressure wave magnitude and wave speed. This is believed due to the air mesh in the MMALE simulations. The waveform and speed have been found to be very sensitive to the density of air mesh. A comprehensive mesh sensitivity study will be conducted in the next reporting period. Besides, the pressure traces predicted by MMALE exhibited double peaks. The second peak should be caused by the dynamic pressure, which has a lower speed compared to the shock wave. It should be noted that with the change in the design of the support structure and the use of a gantry, the effect of reflection will be even smaller. However, a simulation of the new support system will be carried out.

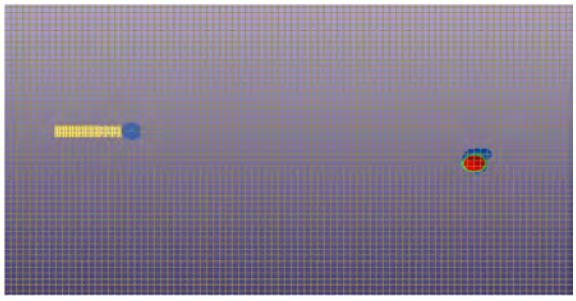

t=0.10 ms

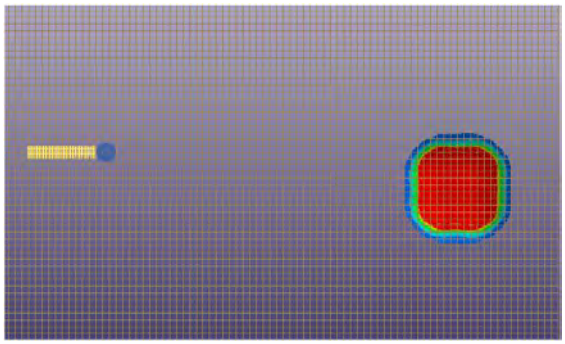

t=0.22 ms

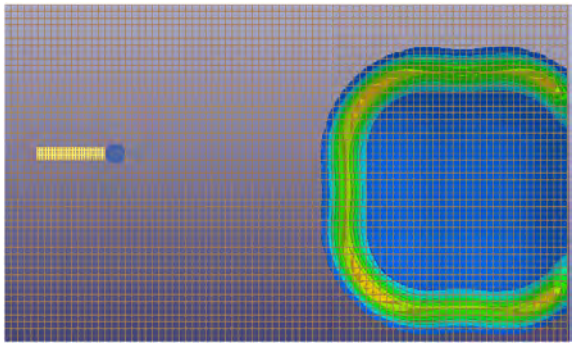

t=0.7 ms

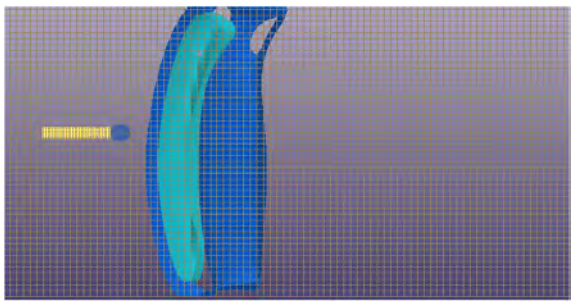

t=2.6 ms

Figure 38. The simulated blast loading events for the case without fixture at the different time points

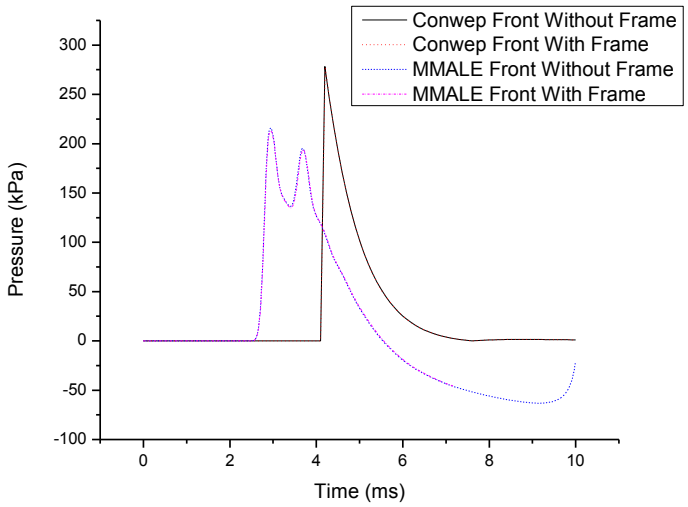

(a)

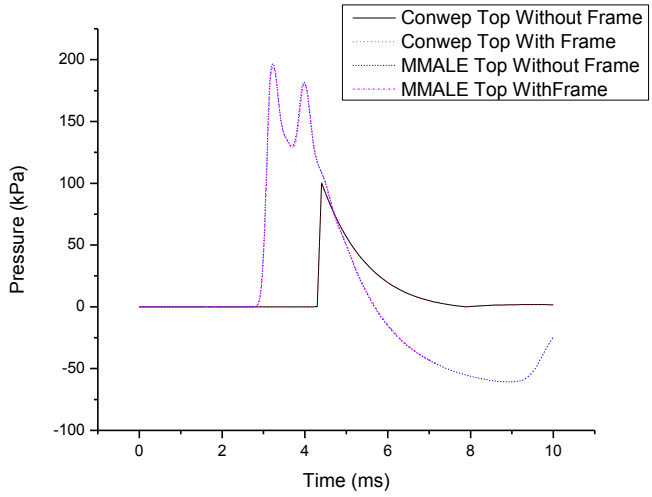

(b)

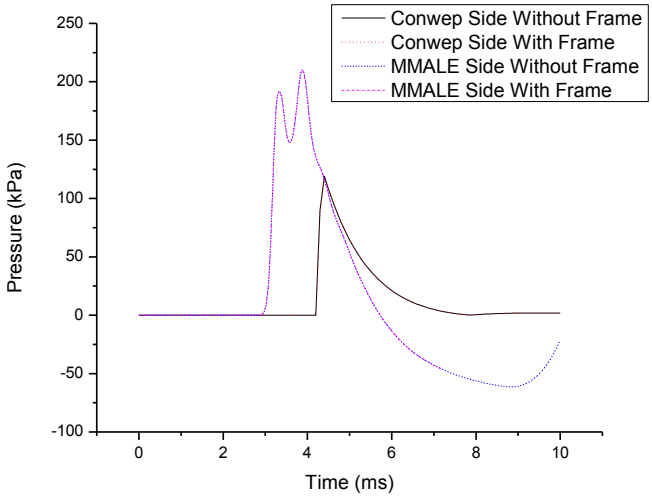

(c)

Figure 39. Model predicted pressure – time histories on the frontal, top and left surface of the pig head

TASK IV REPORT

Task IV - Develop and validate a computer model of the human brain simulating the effects of a blast over-pressure

1. Computer model of the human brain simulating the effects of a blast overpressure

A human head model capable of simulating the effects of blast overpressure on the brain was refined and exercised by conducting a number of open field blast simulations to understand the influence of numerical parameters on head model responses in order to improve the performance of the head model. This detailed FE human head model has been partially validated against cadaveric intracranial pressure generated by a shock tube (Sharma and Zhang, 2011) and it has been recently used to investigate brain responses with and without a combat helmet in open field blast conditions (Zhang et al., 2013). The current studies included: (a) coupling of Lagrangian and Eulerian method using fluid structure interaction (FSI) techniques; (b) validating the head model against head acceleration data from open field blast test results; and (c) studying the effect of changes in head material properties on brain responses to blast overpressure loading.

(a) Investigation of fluid-solid coupling between the blast wave and the human head

FSI is an important coupling interface technique that allows the coupling of Lagrangian, Eulerian and Arbitrary Lagrangian Eulerian (ALE) finite element algorithms in a single model. The leakage of the energy transformation between the ALE mesh and Lagrangian mesh needs to be minimized and controlled. Hypothetically, it is ideal to use similar element sizes for Lagrangian and Eulerian mesh for proper FSI coupling. The current FE human head model has an average element size of 3-4 mm on the surface of the head. An ALE air mesh convergence study was therefore performed by comparing the pressure levels in the models with different element sizes before finalizing the model simulating the human head in an open field blast.

Five air models were meshed with five different element sizes (20 mm, 14 mm, 10 mm, 7 mm and 4 mm). The air mesh encompasses the explosive, head model and and the space between the explosive and the head model. A non-reflecting symmetry boundary condition was applied to 1/4 of the explosive and air, and nodal coupling was assured at the interfaces between the explosive and air mesh. The incident side-on pressure was about 450 kPa based on Bowen's lung damage curve. The detailed blast simulation methodology was described in our previous publication on human head response to blast (Sharma and Zhang, 2011; Zhang and Sharma, 2010, Zhang et al., 2013).

Figure 40 shows the effect of varying air element size on coupling pressure magnitude as well as coup intracranial pressure. For the mesh with 20 mm size, the FSI showed quite a weak coupling which improved with increased mesh resolutions (red hot spot of the pressure contour). As shown by the curves, coupling pressure increased markedly as element size was reduced from 20 to 10 mm. However, this change became less

noticeable as element size changed from 10 to 4 mm. The overall change in pressure magnitude from the 10-mm mesh size to that of 7 and 4 mm was less than 10%. These mesh convergence results suggested that an air model with a 10-mm resolution would be adequate to ensure energy transfer between the blast wave and structure. Also, the model with a 10-mm element size reduced the computational time and resources needed by over 100%, in comparison with higher resolution models.

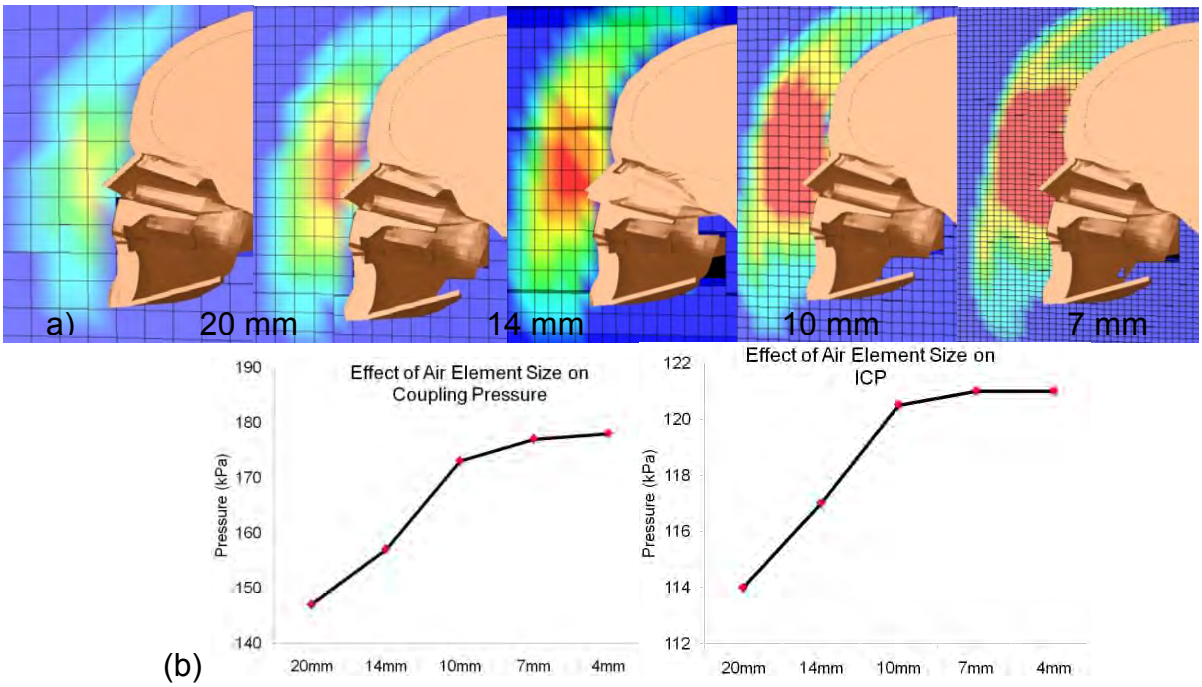

Figure 40: (a) Air blast overpressure contour patterns associated with the use of various air element mesh sizes; (b) Convergence of coupling and intracranial pressure solution as a function of the mesh resolution

(b) Validation of head acceleration responses against open field blast experimental data

Williams (2004) conducted various open field blast experiments using a Hybrid III (HIII) dummy and a newly developed blast headform (MABIL). The instrumented HIII was exposed to a blast from 5 kg of C4 detonated at a height of burst (HOB) of 1.5 m and at standoff distances of 3, 3.5 and 4 m. The acceleration was recorded at the CG of the dummy head. A cylindrical C4 charge was used in the experiments with an aspect ratio of 1:1. The blast test conditions were simulated using an FE human head model and head responses were compared with experimental data. The coupled MMALE and Lagrangian algorithm along with the FSI technique was used to simulate the wave propagation and its interaction with the head model.

Figure 41a shows a comparison of peak head acceleration at three standoff distances between the average experimental data and model results. The predicted peak accelerations were in good agreement with the experiments. Figure 41b shows the comparison of head acceleration-time histories between experimental and simulation results for the 4-m standoff distance. The overall initial pulse durations were similar between the simulation and experiment. The deviation can be due to large variability in

reported experimental data for the same test conditions. It can also due to the fact that a spherical charge was modeled in the simulation whereas cylindrical charges were used in the experiments even though the charge height to diameter ratio was 1.

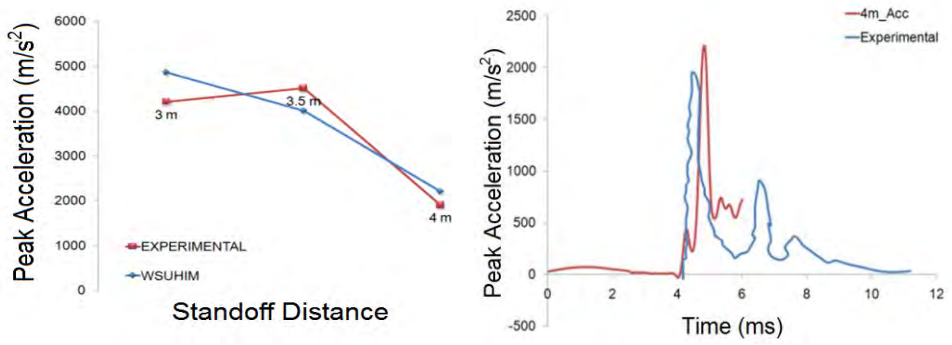

Figure 41: (a) Peak head acceleration between experiment and simulation results; (b) Acceleration-time history comparison (4 m standoff distance)

(c) Effect of changes in brain material property on blast induced brain responses

The bulk modulus of the brain provides compressive resistance against the applied pressure. It can be defined as the increment in pressure per unit volume. The experimentally reported bulk modulus of brain is in the range of 0.128 to 2.5 GPa and this range of values was also used in FE models (McElhaney et al, 1976; Brands et al, 2002; Zhang et al., 2001, Zhang et al., 2013). To analyze the effect of changes in brain bulk modulus on shock induced brain pressure, the model was run with values of 0.5 and 0.12 GPa and the brain response (ICP) was compared to that of the baseline head model in which the modulus used was 2.19 GPa.

It was noted that bulk modulus affected peak brain pressure within a certain range. This effect was found to be dependent upon the different brain regions. The ventricles, parietal cortex and occipital cortex had an increase in ICP with increases in brain bulk moduli, while the frontal cortex ICP was reduced with decreases in bulk moduli. In other words, decreasing the bulk modulus can reduce the ICP in the frontal region and can increase it at other locations. It was also found by Moss et al (2009) that a reduction in bulk modulus can reduce the shock speed and increase the penetration of pressure waves inside the brain. This could be the reason why the deeper locations showed higher pressures in the brain with a reduced bulk modulus.

Blast wave transmitted at very high rate which could exceed the strain rate of 100 s^{-1} as seen in blunt impact. The effect of the higher strain rate properties of brain on the brain responses to blast loading was therefore evaluated. Lippert et al (2004) tested brain tissue int the higher-frequency range of 100 kHz to 10MHz, using the "wave-in-a-tube" ultrasonic method. They found changes in shear moduli in the wide range. Shear moduli (G_0: 1,250 kPa; G_∞: 250 kPa) at 100 times the value of the baseline model were studied and responses to open field blast were compared with those of the baseline model.

The comparison showed that, at all locations, the brain experienced a similar level of peak pressure, suggesting insensitivity of the brain pressure to deviatoric properties of

the brain. The strain responses in the brain cortex were highly sensitive to the changes in shear moduli. In contrast, the strain in the central part of the brain was insensitive to the property change in shear (Figure42).

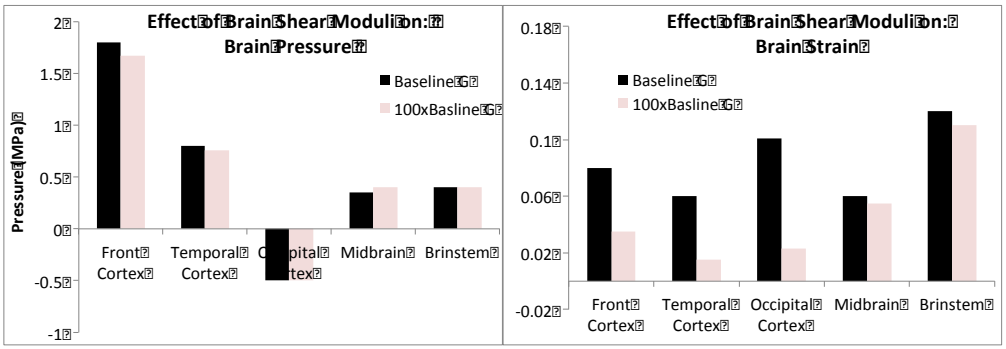

Figure 42. Intracranial pressure and brain tissue strain changes in response to the changes in brain shear properties

2. Investigation of overpressure and impulse profiles as a function of explosive charge weight and standoff distance

According to the proposed blast experiment plan, we will subject the animals and human cadavers to three blast overpressure levels (400, 250 and 150 kPa). To produce these desired peak overpressures (side-on incident pressure) using C4, two test design approaches were compared. Approach A was to use a fixed-weight charge, such as, 8 lb of C4 (equivalent to 5.19 kg of TNT), and place the head of the test subject at three different horizontal standoff distances from ground zero. Approach B was to place the head at the same standoff distance and vary the charge weight to achieve the desired pressure peaks. Although these desired peak pressure levels can be achieved with either approach, the impulse (positive phase impulse) equivalency from the two conditions could be different. Impulse has been considered as one of the important blast parameters responsible for structural or brain damage. The results of our previous studies using a simplified head model (W81XWH-08-1-0678 DoD report, 2009) concluded that at the same peak overpressure, increasing levels of impulse resulted in significantly higher tissue stress waves in the brain as well as greater head acceleration, velocity and displacement. The results also suggested that for relatively short duration blasts (0.5 - 3 ms) the damage effect on the brain component was strongly dependent on impulse, which represents the transfer of momentum to the body/tissue.

The existing semi-empirical models, such as CONWEP, are extensively used to predict the magnitude of the peak pressure and impulse delivered to a target. Since the CONWEP model has been implemented in LS-Dyna (LSTC, Livermore, CA), a commercial finite element code, we first used cubic root scaling to determine the scaled distance and charge weight required to achieve the three pressure levels. The LS-Dyna simulation was then performed based on a spherical air burst model (without reflection) to verify the pressure and further adjustment of the distance and weight was done to obtain the desired peak overpressure levels. The positive phase impulse was calculated based on overpressure time history which is the area under the pressure curve for the duration of the positive overpressure.

Table 5 summarizes the required standoff distances and associated charge weights for the two approaches. Table 6 summarizes the calculated impulse values associated with three peak overpressure levels as a result of using the two different approaches (A, B1 and B2). Figure 43 shows the overpressure time histories with peak pressures of 400, 250 and 150 kPa and their corresponding impulses as a result of 8 lb of C4 charge being detonated at the three standoff locations (Table 5). Figure 44 shows the overpressure time histories and their corresponding impulses as a result of using different explosive weights of C4 detonated at the two selected standoff distances (2.5 m and 3 m). Between B1 and B2, the longer duration of overpressure resulted in higher impulse in B2 as compared to B1. In case of Approach B, different charge weights will be needed which may add additional variables (due to packing) to the blast profile than using a fixed charge weight as proposed in Approach A. The use of approach A appears to be a relative simple way of studying the relative contribution of impulse and peak overpressure to blast-induced brain injury.

Table 5: Required standoff distances and charge weights for two approaches

		Calculated	**400 kPa**	**250 kPa**	**150 kPa**
A	Fixed charge weight at 8lbs	Standoff distance	2.47 m	3.06 m	3.85 m
B1	Fixed standoff distance at 2.5 m	Charge weight	5.2 kg	2.75 kg	1.4 kg
B2	Fixed standoff distance at 3.0 m	Charge weight	9 kg	4.8 kg	2.4 kg

Table 6: Impulses from two different approaches

	Impulse (kPa_s)	**400 kPa**	**250 kPa**	**150 kPa**
A	Fixed charge weight at 8 lb	0.22	0.18	0.14
B1	Fixed standoff distance at 2.5 m	0.21	0.14	0.09
B2	Fixed standoff distance at 3.0 m	0.25	0.17	0.11

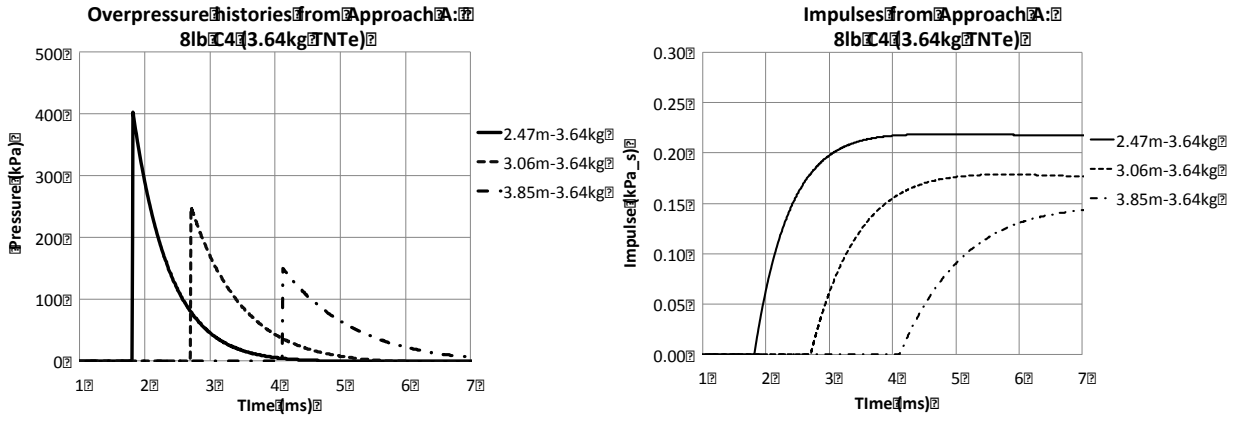

Figure 43. Overpressure and impulse time histories using Approach A.

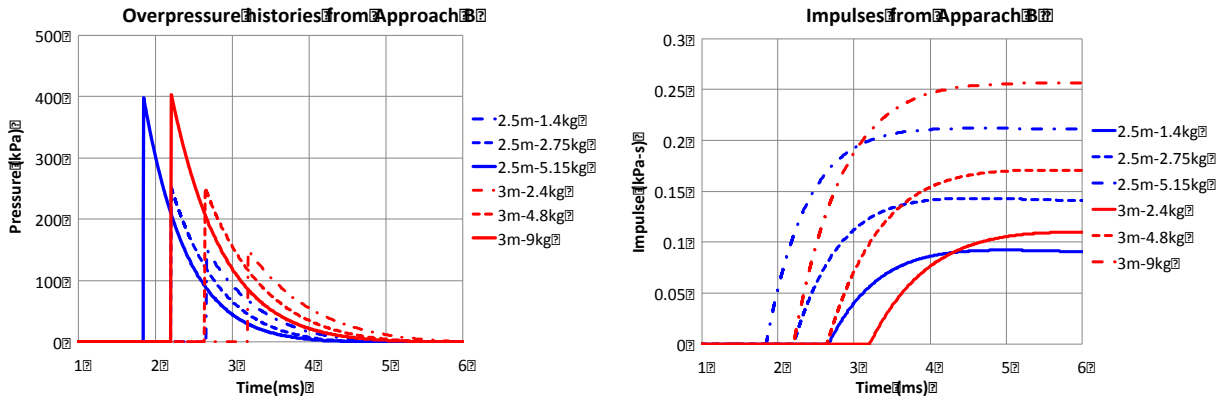

Figure 44. Overpressure and impulse time histories at three peak pressure levels using Approach B.

3. Determination of the Mach stem region and the required height of burst (HOB)

For our blast test design, the blast wave is produced by a free air burst with a relatively small explosive charge (3.63 kg of C4). Therefore, the "triple point" path as a function of HOB needs to be determined first in order to properly locate the Mach stem region/irregular reflection region and regular reflection region at the corresponding standoff distances. The "triple point" is the path where the incident wave, reflected wave and Mach stem meet (Figure 45a). It is known that below the triple point, in the Mach stem region, the overpressure has a single peak when the reflected wave merges with the incident wave (Figure 45c). Above the triple point, in the normal reflection region, the overpressure has two peaks because the reflected wave does not merge with the incident wave (Figure 45b). It is desired to subject the test specimen to a single shock front where the Mach stem is located because above it the test subject will be exposed to two peaks. Exposure to two peaks would complicate our analysis of injury mechanism and tolerance.

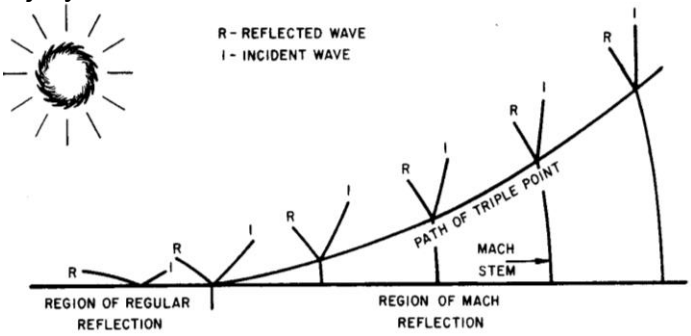

(a) Path of triple point

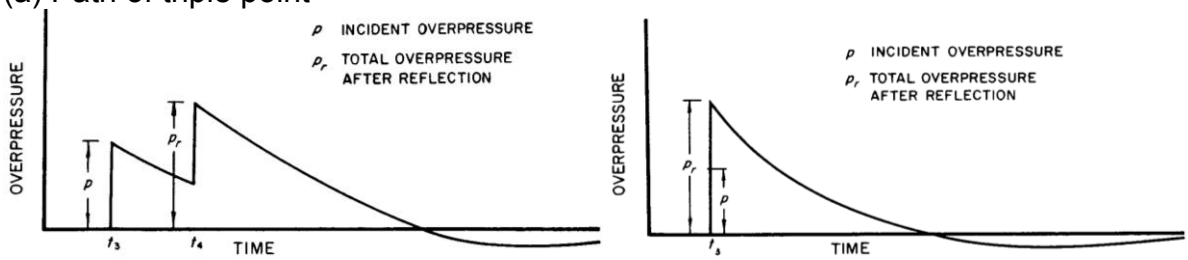

(b) Overpressure in the regular reflection - incident and reflected waves do not merge

(c) Overpressure in the Mach stem region - reflected wave merges with incident wave

Figure 45. Mach stem, triple point and overpressure profiles.

Figure 16 shows a plot of the scaled height of the triple point as a function of a range of scaled heights of burst and for a range of scaled standoff distances. For example, using 1 lb of explosive (W=1 lb), and a HOB of 3 ft, the triple point is 3 ft high at a standoff distance of 12 ft. That is, to receive a blast wave with a single peak for a HOB of 3 ft above ground zero and with the test subjects located 3 ft above ground, the standoff distance needs to be 12 ft or more. The overpressure time histories at that standoff distance can then be computed using LS-Dyna to verify the single peak profile (Figure 4747). The calculation will be further verified with the actual measurements during the upcoming test readiness run.

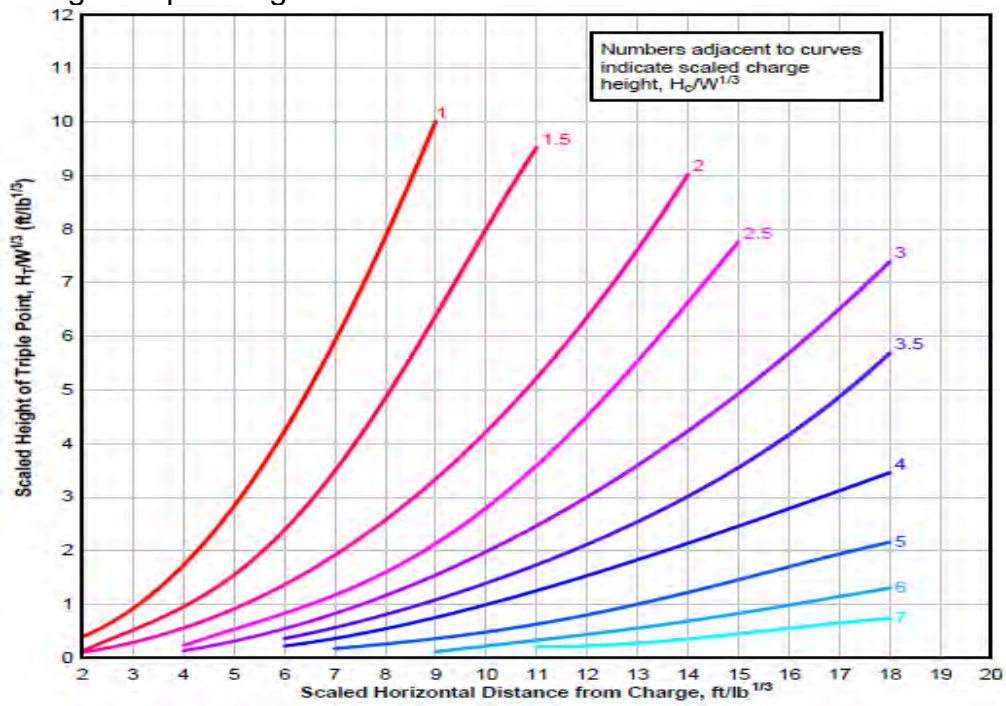

Figure 16. Scaled height of triple point using empirical equation.

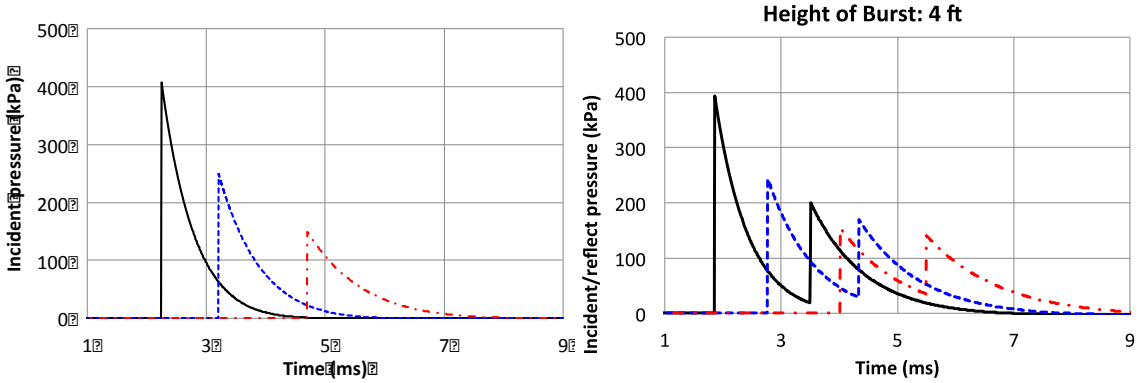

(a) (b)

Figure 47. LS-Dyna COMWEP calculated: a) Single wave profiles (Mach region) at three standoff distances from a free air burst at 3 ft above the ground zero, b) Two wave fronts at a HOB of 4 ft.

4. Open field blast test layout plan

Figure 48 shows one possible layout of open field blast testing to be conducted at ARES/TW test site. For each test day, the two test subjects are either an instrumented pig paired with a non-instrumented pig or an instrumented cadaver paired with a non-instrumented pig. The test subjects will be supported by a 10' x 12' gantry. The high-speed cameras and data acquisition system will be protected by custom-made steel shields from blasts and fragments. The protected recording systems will be placed no more than 30 ft away from ground zero to reduce the noise generated from long cables. Foam blocks will be placed under the data acquisition system and camera stands to isolate the ground shock propagated along the concrete floor. The test team will be located either about 100 ft away from the charge or 50 ft behind the concrete wall to remotely control the recording systems before the detonation of the explosives. The test site ambient conditions of pressure, temperature and wind velocity will also be monitored.

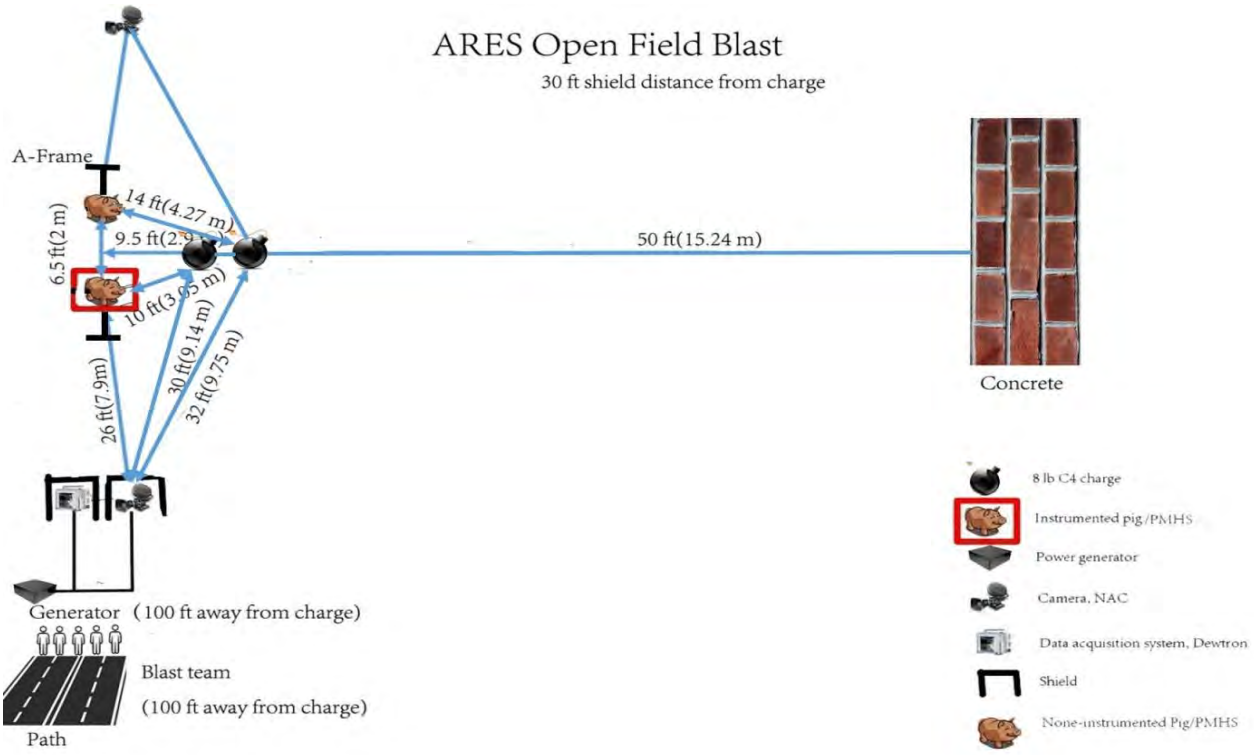

Figure 48. Schematic diagram of blast test layout.

The week of July 22, 2013 is the scheduled time for our test readiness runs (TRR) at ARES with the help of the Team Wendy blast team. At the TRR, a number of pencil probes will be used to verify the blast overpressure magnitude and Mach stem waveform from a range of standoff distances, burst heights and specimen heights to finalize the test set up.

5. Human head model and eye model development/integration

With increasing frequency of eye injuries, it behooves us to incorporate into our human head model a realistic model of the eye so that we can study the potential of injury to the retina and optic pathway induced by blast overpressure and its association with

neural and axonal injury occurring in other regions of the brain. This effort involves the following subtasks:

(a) Literature review of blast induced ocular injury and TBI
(b) Development and integration of the eye model with the human head model
(c) Validation of the eye model against cadaveric impact test data

(a) Literature review of blast induced ocular injury and TBI

From 2002 through 2007, during Operations Iraqi Freedom and Enduring Freedom (OIF/OEF), 13% of wounded U.S. soldiers sustained significant combat ocular trauma requiring evacuation (Weichel et al. 2008; Blanch et al. 2011). Combat ocular trauma is frequently associated with polytrauma in 85% of cases with 66% cases with traumatic brain injury (TBI). The traumatic brain injury severity associated with ocular injury included mild TBI (31%), moderate TBI (30%), severe TBI (25%), and penetrating TBI (14%) (Weichel et al. 2009).

The rate of TBI was higher in soldiers with closed-globe (75%) than open-globe injuries (57%). In closed-globe injury, the common injury pattern was a unilateral zone 3 injury (50% of closed-globe) without any laceration on outside of eye or any zone 1 injury. Weichel et al. (2009) also reported that globe rupture occurred in 4% of the total ocular trauma without zone 1 damage. The data suggested that injury to the globe may be due to anterior-posterior compression of the globe and raising intraocular pressure to a point that the sclera tears. The documented use of eye protection was only 24% among all 523 ocular injury cases (Weichel et al. 2008). The eye region remains vulnerable to blast trauma.

A literature search revealed only one published study of a 3-D computer eye model to evaluate the influence of facial features on blast wave loading on the human eye (Bhardwai et al., 2013). Due to the lack of detailed vitreous body and other components within the cornea /surface of the eyes, the internal pressure change was estimated from the surface corneoscleral stress. The model also lacks skull and brain structures. As such, this model is incapable of investigating the relationships between the ocular injury and brain injury due primary blast exposure.

By integrating our detailed eye model with our improved computer model of the human head for blast simulation, the biomechanical cause and effect relationships between combat ocular trauma, optic nerve injury and mild traumatic brain injury due to primary blast exposure can be investigated.

(b) Development and integration of the eye model with the human head model

A few FE models were developed to simulate retinal surgical procedure (Sawusch and McDonnell, 1992). Uchico et al. in 1999 presented the first FE modeling of blunt trauma of human eye. Although these early study included important corneosclera variable thickness information, the inner essential components such as lens, optical nerve and fluid were not included. Stitzel et al. in 2002 developed a detailed FE model of eye known as Virginia Tech Eye Model (VTEM) for blunt impact. VITM was partially

validated against both mild and severe experimental eye impact conditions. VITM included some of the important components of eye such as lens, zonules, ciliary body, aqueous and vitreous, however the orbital cavity was simplified and the optical nerve and six extraocular muscles were not included.

The geometry and mesh of the human eye have been developed at WSU before the project started. The data were obtained from an anatomical atlas and from the literature (Woo et al., 1972, Uchio et al., 1999). This detailed eye model included all essential components of the eye: the cornea, sclera, vitreous and aqueous humor, lens, zonules, ciliary body, retina, extraocular muscles, and optic nerve (Figures 49 and 50). In the current project period, the geometry and mesh pattern of the roof, wall and floor of the orbit (frontal, ethmoid, lacrimal, maxillary, zygomatic, sphenoid bones) in the current WSU human head model was modified and improved to provide proper mesh connectivity with the eye globe. The fatty tissues surrounding the eyes were also developed to fill in the cavity between the globe and improved orbital cavity of the skull (Figure 50). The direct node-to-node connections were assured between the eye/fat and fat/orbit interface to avoid the use of a contact interface, to achieve more stable numerical results and to reduce computational cost. The model was made up of over 28,000 elements with more than 95% being of hexahedral solid elements.

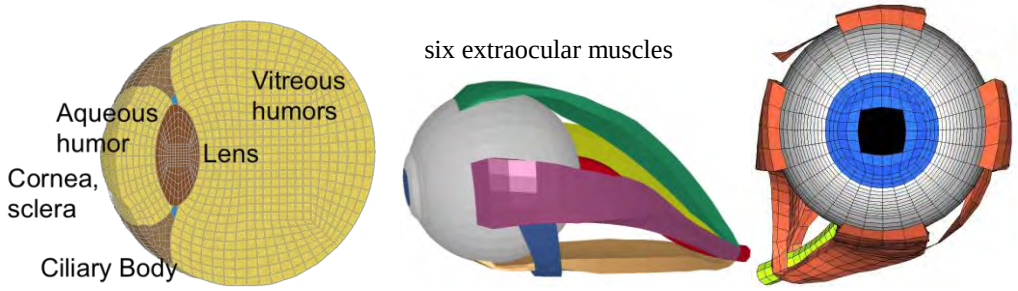

Figure 49. The essential components of the human eye model

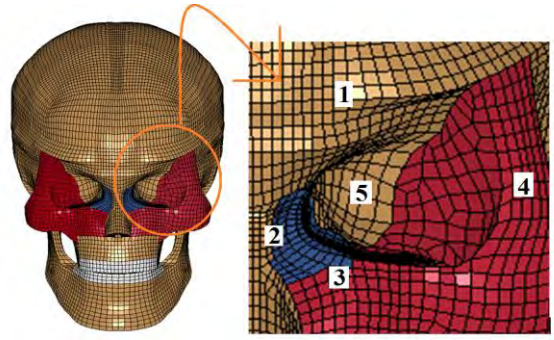

Orbital cavity modification


Transverse view of eye within the orbital cavity

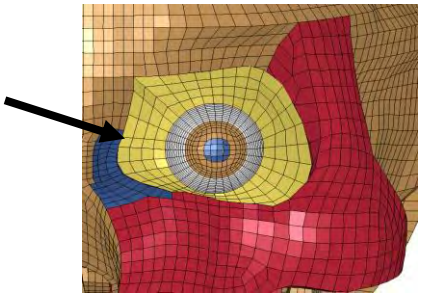

Figure 50. Integration of the eye model with the head model with the direct node connections between the fatty tissues surrounding the globe and orbit cavity surface of skull/facial model.

(c) Validation of the eye model against cadaveric impact test data

We believe that validating mechanical responses predicted by the eye model against experimentally measured results from cadaveric tests conducted on eye injury is an essential step to assure the validity and accuracy of a numerical model for predicting a range of physical phenomena. Even though the cadaveric tests we simulated were blunt impact and not primary blast loading, the impact speeds involved are quite high and the exercise will be beneficial to the development of a model simulating blast loading. Most importantly, the validation process will help improve the numerical performance of the model such as its numerical stability and realistic deformation mode, among others. Experimental data reported in literature (Stitzel et al., 2002) were used to validate the current FE eye model, as shown in Table 7.

Table 7: Eye impact validation cases

Impactor	BB		Baseball		Foam			
Velocity	92m/s	56m/s	34.4m/s	41.2m/s	30m/s	10m/s	14.3m/s	28.6m/s
Mass (g)	0.375	0.375	146.5	146.5	0.077	0.077	0.077	0.077

Validation results

When the displacement of the frontal aspect of the eye in the coronal plane was compared with experimental data, we found reasonable correlation (Figure 51). Figure 52 compares model predicted deformation pattern to the experimentally observed deformation on eye specimens. The model predicted pattern matched the data quite well.

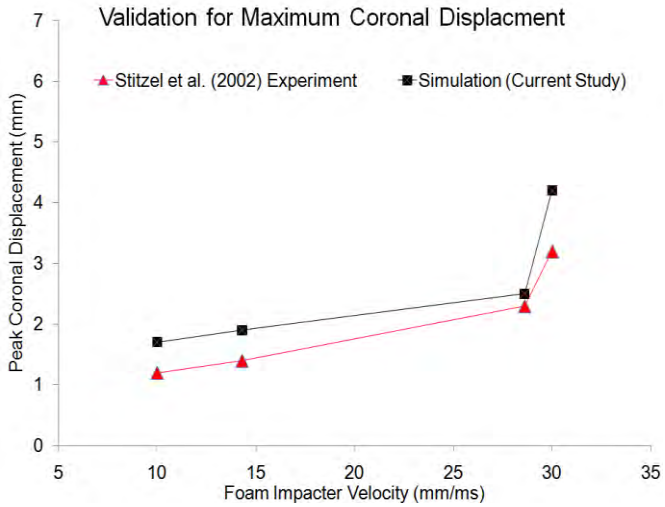

Figure 51. Model prediction vs experimentally measured maximum coronal displacement of the eye from foam impact at various velocities

Ocular pressure responses

Ocular pressure was also studied from all of validation cases. Figure 53 shows pressure time histories predicted for the aqueous humor at the front of the eye and the lens. The highest pressure response was found for BB impact at 92 m/s where the frontal ocular site sustained a higher pressure than the lens. Pressure propagation through the eye globe for all three severe impact cases is shown in Figure 54. For the BB case, high pressure was induced at the cornea followed by the aqueous humor and lens. Because of small shape of the BB, the pressure hot spot was concentrated around the impactor site. For foam impact, high pressure propagated to the aqueous humor and lens without affecting the vitreous humor. In the case of baseball impact, high pressure was produced throughout the globe. Additionally, the zonules and ciliary body, the binders of lens anatomically, both experienced high tensile stresses.

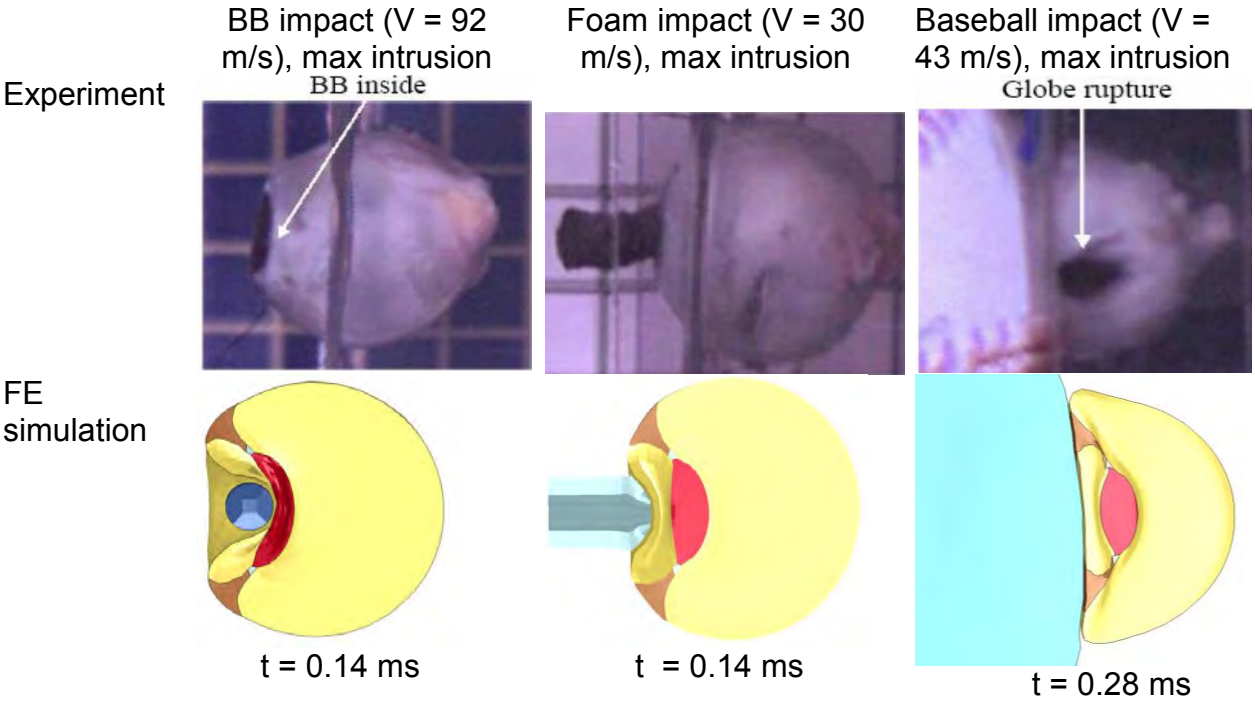

Figure 52. Maximum eye globe deformation captured during BB, foam, and baseball impact on the eye at various velocities

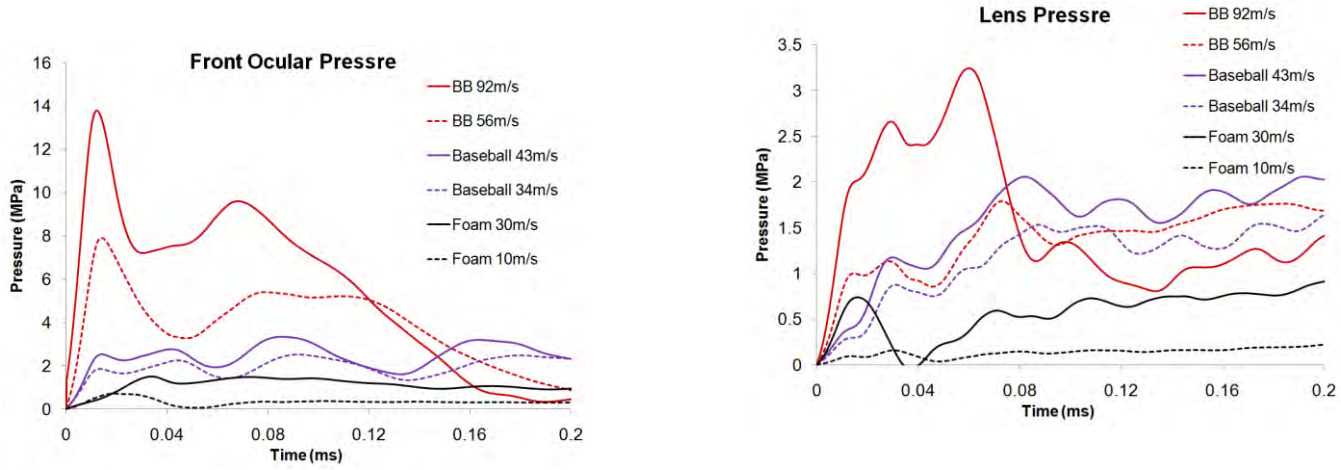

(a) (b)

Figure 53. Comaprsion of ocular pressure time histories for (a) front of the eye and (b) lens due to mild and severe impact.

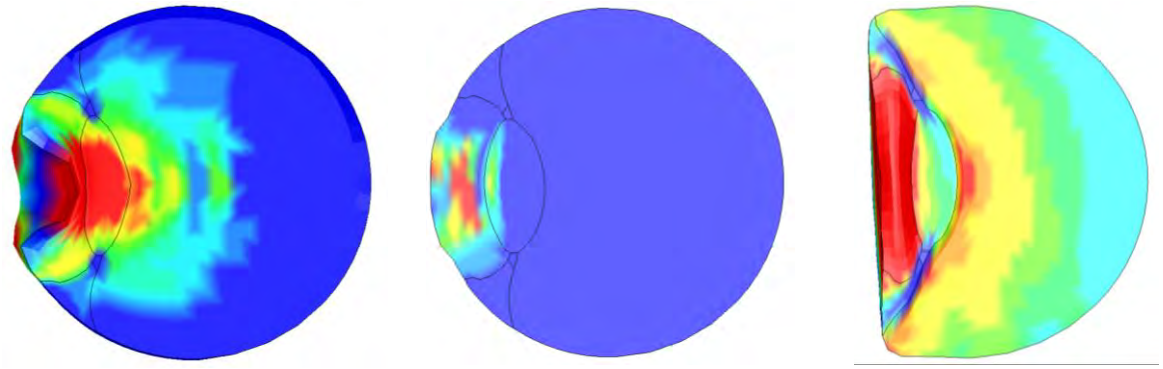

(a) t = 0.07 ms (b) t = 0.03 ms (c) t = 0.20 ms

Figure 54: Pressure propagation inside the eye during (a) BB, (b) Foam, and (c) Baseball impact at different instants of time.

Future work

- To refine eye model by alteriing the element size and improving the mesh quality.
- To complete the human head model refinement: segregate the anatomical structures, such as the corpus callosum, thalamus, basal ganglia and differential white matter and the gray matter in the cerebellum so that the heterogeneous, regional and anisotropic material properties can be incorporated to fully understand localized responses in blast TBI.
- To perform FE simulation to predict the blast overpressure in air and compare model results to pressure data to be measured from pencil probes in the open blast test.

- To perform FE simulation using human head/eye model to predict the blast overpressure in the brain/eye and validate the model results against the experimentally measured pressure data in the cadaver head from open field blast testing.

CONCLUSIONS

1. Preparation for the open air blast tests on swine and PHMS are on schedule and almost complete. Tests will begin in October, 2013 pending receipt of Kulite pressure transducers which are promised for delivery in August 2013. A test readiness run is scheduled for the week of 22 July, 2013
2. Development of the brain models for the swine and human are on schedule. The models are ready to be validated after we obtain data from the blast testing to be done later this year. We will not publish these models until they are validated because publication of unvalidated models can confuse the literature in case the models cannot be eventually validated

REFERENCES

Arbogast KB, Prange MT, Meaney DF, Margulies SS. (1997) Properties of cerebral gray and white matter undergoing large deformation. 7th Injury Prevention through Biomechanics Symposium, Detroit, Michigan, USA; pp. 33–40.

Bhardwaj, R., K. Ziegler, J. H. Seo, K. T. Ramesh, and T. D. Nguyen. (2013) A computational model of blast loading on the human eye. Biomechanics and Modeling in Mechanobiology. 1-18.

Brands, D. W., Bovendeerd, P. H., and Wismans, J. S. (2002) On the potential importance of non-linear viscoelastic material modelling for numerical prediction of brain tissue response: test and application. Stapp Car Crash J, 46:103-121.

Browne, K. D., Chen, X. H., Meaney, D. F. & Smith, D. H. (2011) Mild traumatic brain injury and diffuse axonal injury in swine. Journal of Neurotrauma **28**:1747-1755.

de Lanerolle NC, Bandak F, Kang D, Li AY, Swauger P, Parks S, Ling G and Kim JH (2011). Characteristics of an explosive blast-induced brain injury in an experimental model. Journal of Neuropathology and Experimental Neurology, 70:1046-1057.

Fritz, H. G. *et al.* (2005) A pig model with secondary increase of intracranial pressure after severe traumatic brain injury and temporary blood loss. Journal of Neurotrauma **22**:807-821.

Gyorgy A, Ling G, Wingo D, Walker J, Tong L, Parks S, Januszkiewicz A, Baumann R, Agoston DV (2011) Time-dependent changes in serum biomarker levels after blast traumatic brain injury. Journal of Neurotrauma 28:1121-1126.

Kallakuri, S. *et al.* (2012) Impaired axoplasmic transport is the dominant injury induced by an impact acceleration injury device: An analysis of traumatic axonal injury in pyramidal tract and corpus callosum of rats. Brain Research 1452:29-38,

Li, Y., Zhang, L., Kallakuri, S., Zhou, R. & Cavanaugh, J. M. (2011) Quantitative relationship between axonal injury and mechanical response in a rodent head impact acceleration model. *Journal of Neurotrauma* **28**, 1767-1782.

Lippert, S. A., Rang, E. M., and Grimm, M. J. (2004). The high frequency properties of brain tissue. Biorheology, 41(6):681-691.

Mao H, Zhang L, Yang KH, King AI. (2006) Application of a finite element model of the brain to study traumatic brain injury mechanisms in the rat. Stapp Car Crash Journal 50:583–600.

McElhaney, J. H., Roberts, V. L., and Hilyard, J. F. (1976). Handbook of human tolerance. Japan Automobile Research Institute, Inc.

Moss, W. C., King, M. J., and Blackman, E. G., (2009) Skull flexure from blast waves: a mechanism for brain injury with implications for helmet design. Physical Review Letters, 103(10), #108702.

Saikali S, Meurice P, Sauleau P, Eliat PA, Bellaud P, Randuineau G, Vérin M, Malbert CH (2010).A three-dimensional digital segmented and deformable brain atlas of the domestic pig.J Neurosci Methods. 192(1):102-109.

Sajja VS, Galloway MP, Ghoddoussi F, Thiruthalinathan D, Kepsel A, Hay K, Bir CA, Vandevord PJ (2012) Blast-induced neurotrauma leads to neurochemical changes and neuronal degeneration in the rat hippocampus. NMR Biomed 25:1331-1339.

Saljo, A., Arrhen, F., Bolouri, H., Mayorga, M. & Hamberger (2008) A. Neuropathology and pressure in the pig brain resulting from low-impulse noise exposure. Journal of Neurotrauma 25:1397-1406, doi:10.1089/neu.2008.0602.

Sawusch, M. R., and McDonnell, P. J. (1992) Computer modeling of wound gap following radial keratotomy. Refract Corneal Surg, 8(2):143-145.

Sharma, S., Zhang, L. (2011) Prediction of Intracranial Responses from Blast Induced Neurotrauma using a Validated Finite Element Model of Human Head. Proceedings of the 7th Injury Biomechanics Symposium, Columbus, OH, USA

Stitzel, J. D., Duma, S. M., Cormier, J. M., and Herring, I. P. (2002). A nonlinear finite element model of the eye with experimental validation for the prediction of globe rupture. Stapp Car Crash J, 46:81-102.

Tamura A, Hayashi S, Watanabe I, Nagayama K, Matsumoto T.(2007) Mechanical characterization of brain tissue in high-rate compression. Journal of Biomechanical Science and Engineering; **2**(3):115–126.

Teland et al (2010a) Numerical simulation of mechanisms of blastinducedtraumatic brain injury. J AcoustSoc Am 127:1790

Teland et al (2010b) Numerical simulation of mechanisms of blastinducedtraumatic brain injury. POMA 9:020004.

Uchio, E., Ohno, S., Kudoh, J., Aoki, K., and Kisielewicz, L. T. (1999). Simulation model of an eyeball based on finite element analysis on a supercomputer. Br J Ophthalmol, 83(10):1106-1111.

Viano, D. C., Casson, I. R., Pellman, E. J., Zhang, L., King, A. I., Yang, K. H., (2005) Concussion in professional football: brain responses by finite element analysis: Part 9. Neurosurgery, 57(5):891-916.

Weichel, E. D., M. H. Colyer, C. Bautista, K. S. Bower, and L. M. French. (2009) Traumatic brain injury associated with combat ocular trauma. Journal of Head Trauma Rehabilitation 24 (1):41-50.

Weichel, E. D., M. H. Colyer, S. E. Ludlow, K. S. Bower, and A. S. Eiseman (2008). Combat Ocular Trauma Visual Outcomes during Operations Iraqi and Enduring Freedom. Ophthalmology 115 (12):2235-2245.

Williams, K. (2004). Test plan - MABIL development phase III. Valcartier, Quebec, Canada.

Woo, S. L., Kobayashi, A. S., Lawrence, C., and Schlegel, W. A., (1972) Mathematical model of the corneo-scleral shell as applied to intraocular pressure-volume relations and applanation tonometry. Ann Biomed Eng, 1(1):87-98.

Wood JL (1971). Dynamic response of human cranial bone. Journal of Biomechanics; 4:1–12.

Yang KH, Mao H, Wagner C, Zhu F, Chou CC and King AI (2010) Modeling of the Brain for Injury Prevention in Biomechanics of Brain, Bilston L (ed.), New York: Springer-Verlag.

Zhang, L., Yang, K. H., Dwarampudi, R., Omori, K., Li, T., Chang, K., Hardy, W. N., Khalil, T. B., and King, A. I. (2001) Recent advances in brain injury research: a new human head model development and validation. Stapp Car Crash J, 45:369-394.

Zhang L., Sharma, S. (2010) Computational Modeling of Causal Mechanisms of Blast Wave Induced Traumatic Brain Injury – A Potential Tool for Injury Prevention. Technical Report. Fort Detrick (MD): U.S. Army Medical Research and Material Command

Zhang, L., Makwana, R., Sumit, S. (2013) Brain response to primary blast wave using validated finite element models of human head and advanced combat helmet. Frontiers in Neurology (In press).

Zhu F, Skelton P, Chou CC, Mao H, Yang KH and King AI. (2013) Biomedical responses of a pig head under blast loading: a computational simulation. International Journal for Numerical Methods in Biomedical Engineering, in press.